TECHNICAL PAPER

Investigation on high strain rate response of lightweight sandwich panel with aluminum corrugated core and smart composite facesheets

S. M. R. Khalili[1,2] · R. Maher[3] · P. Mahajan[4]

Abstract

This study investigates experimentally and numerically the performance of lightweight sandwich panels with trapezoidal aluminum corrugated core and composite facesheets reinforced with shape-memory alloys (SMAs) subjected to high strain rate loading. Composite and aluminum samples were prepared to conduct tensile tests, and the requisite data have been obtained during the tests. The composite laminate facesheets made of glass/epoxy were fabricated utilizing the hand-layup approach using 4 layers. For the purpose of reinforcing the composite facesheets, superelastic SMA wires were utilized in three different conditions: 6 SMA wires in the absence of pre-strain, 6 SMA wires with 3 percent pre-strain, and 12 SMA wires with 0 percent pre-strain. The samples were subjected to a high strain rate loading. With the aim of validating and comparing the experimental and numerical results, the samples were modeled in LS-Dyna software, assuming the test condition. This study aims to investigate the influence of adding SMA wires, the quantity and position of SMA wires, and pre-straining the SMA wires in the composite facesheets to enhance the performance of sandwich panels against the high strain rate loadings. The presence of SMA wires results in better energy absorption and the employment of pre-strain results in better high strain rate behavior in sandwich panel at the expense of its weight. The results demonstrate that the absorbed energy from 117.247 J for the samples without the SMA wire was increased to 128.749 J for the 6 SMA wires samples. However, when a pre-strain of 3% was applied to the wires, the energy absorption in the samples with 6 SMA wires increased further to 142.57 J. On the contrary, when the SMA wires were located far from the center of the hitting point, the energy absorbed decreased to 123.12 J for the samples with 12 wires without pre-strain.

Keywords Strain rate · High-speed impact · Composite sandwich panels · Corrugated core · Shape memory alloys

1 Introduction

Sandwich panels with corrugated cores have been increasingly utilized for different structures [1]. Sandwich structures mainly comprise three parts: central core, front (top) facesheet, and back (bottom, rear) facesheet. Due to having low weight compared to high stiffness, sandwich structures develop improved structure properties and high energy absorption [2–11]. In view of the wide application of corrugated core sandwich structures with composite facesheets in making mechanical parts, for instance, in the aerospace industry, understanding the impact properties of the structures, such as energy absorption, is necessary to ensure structural reliability when structures are subjected to loadings and unwanted impacts. A type of sandwich panel structure is the corrugated core composite structure, which has a core with wavy shape. The core separates the skins and improves the vertical force resistance. The sandwich panel

✉ S. M. R. Khalili
smrkhalili2022@gmail.com

1   Center of Research for Composite and Smart Materials and Structures, Faculty of Mechanical Engineering, K. N. Toosi University of Technology, Tehran, Iran

2   Applied Mechanics Department, Indian Institute of Technology, New Delhi 110016, India

3   Department of Mechanical Engineering, South Tehran Branch, Islamic Azad University, Tehran, Iran

4   Applied Mechanics Department, Indian Institute of Technology, New Delhi 110016, India

with a corrugated core behaves like a thick plate, because of its high shear strength. A corrugated core sandwich panel has an advantage over a honeycomb core sandwich panel in that it can withstand bending, twisting and vertical shear forces. This could also enable the large-scale production of such structures for applications that require energy absorption [12].

In recent years, the application of shape-memory alloys (SMA) has captured the undivided focus of researchers due to their unique properties for improving composite structures. Nitinol (NiTi) is one of the first smart materials discovered by W. J. Buehler in 1962 [13]. Nitinol has two crystal phases: the austenite phase, which is strong and exhibits more stability at high temperatures, and the martensite phase, which is soft and more stable at low temperatures [14]. Pseudoelasticity, also known as superelasticity, is the capability of SMAs to restore to their original state at the time of unloading after multiple deformations. This property of SMAs is present at constant deformation and constant temperature. The application of SMAs in science and engineering is on the rise due to their unique characteristics. The composite structures reinforced with SMA are capable of changing their stiffness properties. Moreover, the stress resulting from SMA phase transformation leads to improving the structure strength against high strain rate loads [15]. In this study, the SMA wires with pre-strain are added to composite facesheets of sandwich panels at room temperature.

Recently, the impact response of composite structures has been interested by many researchers [16–20]. Katariya et al. [21] investigated the nonlinear dynamic responses of layered skew sandwich composite structure experimentally and numerically. Cantwell and Morton [22–24] carried out an experimental study of the high and low-speed impact on laminated composites. They showed that a localized deformation state was generated by the projectile which arises from high-speed impact loading, while it was the opposite of the low-speed cases. Tanabe et al. [25] investigated laminates constructed by various reinforced fibers and demonstrated that the mechanical characteristics of the backside layer play a vital role in the point of view of energy absorption. Hazell et al. [26–28] studied the effect of the impact velocity on the energy absorption, and it is demonstrated that the energy absorption accompanied by damage extension was constant for high to higher speed impacts. A comprehensive review of the recent experimental studies on the high-speed impacts of composite materials has been summarized in the latest reviews [29]. The finite element (FE) model of the high-speed impact response of composite laminates has also been studied by many researchers. Gower et al. [30] studied the ballistic impact of composite panels by the FE Model, and the findings were compared with the results obtained from the experimental study on rear surface displacement

and delamination. Their study indicated that an increased in-plane modulus and in-plane strain caused reduced the back face signature (BFS) of woven Kevlar composites. He et al. [31] by considering the response of the composite plate as a function of the impact speed, predicted the penetration depth and the ballistic limited speed. López-Puente et al. [32] forecasted the damaged area in carbon fiber-reinforced polymer (CFRP) woven laminates arisen by normal and oblique ballistic impacts. They investigated the damage on the CFRP plates based on the Chang-Chang damage criterion. The FE model was validated with experimental results. They studied the residual speed and damage area in different velocities of projectile at two different impact angles (0° and 45°). Iváñez et al. [5] suggested a FE Model compare the ballistic response of sandwich panels, which was compared by the experimental results. They demonstrated that the suppression of the foam core caused the ballistic limit to be decreased and the residual velocities were increased (36%) at impact velocities almost equal to the ballistic limit. Wadley et al. [33] investigated the deformation and fracture of sandwich panels with circular corrugated cores subjected to high-speed impact loadings. Kılıçaslan et al. [34] investigated and proposed the finite element approach for modeling the impact on sandwich structure with trapezoidal corrugated aluminum core with aluminum facesheets. They showed that the panels impacted with a conical striker with a 0°/90° layer orientation had relatively less energy absorption than a 0°/0° orientation panel. Quanjin Ma et al. [35] conducted a review study of some recent trends on the impact response of sandwich panels and core structures.

Smart materials such as shape memory alloys (SMAs) have attracted the attention of many researchers in recent years due to their unique properties to improve the response of composite laminates and sandwich panels against impact loads. Khalili et al. [36, 37] focused on examining the effective parameters influencing smart hybrid composite plates subjected to low-speed impact. They investigated the effect of SMA wires on the stiffness of structures. Their study showed that the use of SMA wires in unidirectional composite plates enhances the global properties of hybrid composite plates. The composite plates with SMA wires dump energy much more rapidly and uniformly than the composite plates without SMA wires. Eslami-Farsani et al. [38] assessed the effect of volume fraction and pre-strain of SMA wires on the behaviors of composite laminates reinforced with SMA subjected to high-speed impact. They found that as the volume fraction of the wires increased, the energy absorbed by the laminate decreased. On the other hand, pre-strain application leads to residual stresses in the samples. Verma et al. [39] investigated the influence of high-speed impact on the composites reinforced with SMA. They considered the configuration of SMA wires located between the composite layers. The results revealed that the meshed SMA absorbs
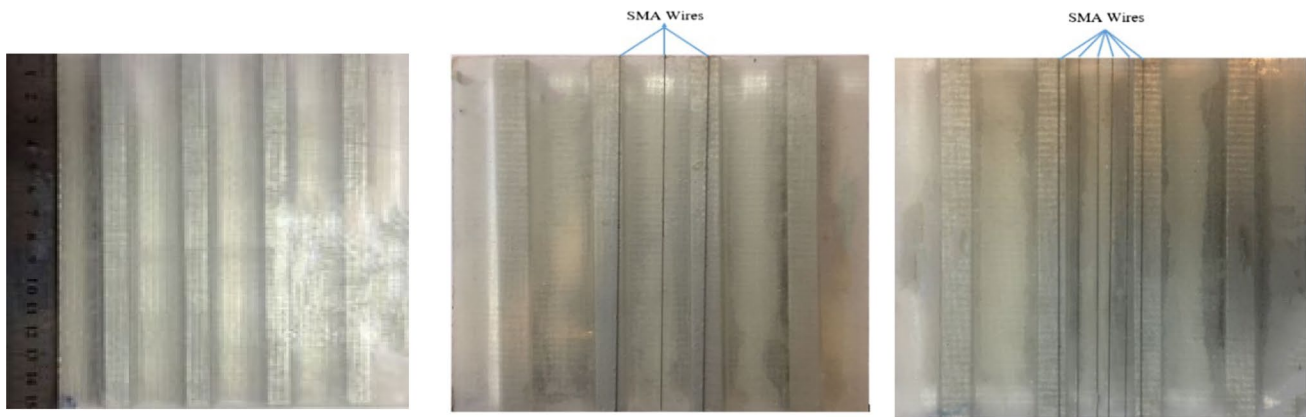
Fig. 1 Samples geometry

more energy than the normal one. Rogers et al. [40] analyzed the damaged area induced by the high-speed impact on composites reinforced by SMA. The results showed that high-speed impact leads to a more local damaged area compared to low-speed impact.

The present study is innovative as it explores the effect of adding SMA wires in composite facesheets of corrugated core sandwich panels subjected to high strain rate loading, which to the best of the author's knowledge, less work has been addressed previously. In this research work, the response of sandwich panels with corrugated core and composite facesheets subjected to high strain rate impact are explored numerically and experimentally. Additionally, the effect of adding superelastic shape memory alloys to composite facesheets are examined to understand the possible improvement of structure properties, when subjected to high strain rate tests. Using LS-Dyna commercial code and modeling the sandwich panel, other parameters are also examined including the number and position of wires, and the influence of applying the pre-strain to the SMA wires.

2 Experimental procedure

2.1 Samples preparation

In this study, the sandwich panel was made of four parts: aluminum corrugated core, front and back composite facesheets, and SMA wires (Fig. 1).

Due to having low density, high flexibility as well as acceptable strength, aluminum is being widely used in engineering applications. In this study, aluminum grade 3000 with 0.3mm in thickness is used to make corrugated cores. To make trapezoidal corrugated cores, a steel mold with desired size and corrugated angles was used. Figure 2 shows the geometry of the trapezoidal corrugated core cross section. Figure 3 shows the aluminum corrugated core samples.
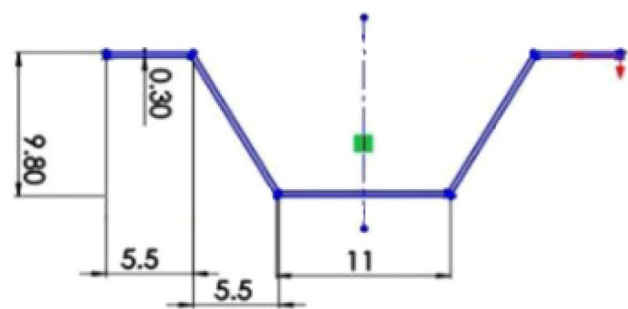

Fig. 2 The aluminum corrugated core geometry

Fig. 3 The aluminum trapezoidal core sample

Composite facesheets were prepared through the hand layup method at room temperature. The facesheets were made by continuous woven glass fiber/epoxy. To make the composite laminates for facesheets, EPON828 epoxy resin was mixed with 10% hardener and then combined with woven glass fabric (Camelyaf /Turkey). The facesheets laminates' thickness is one millimeter, comprised of four
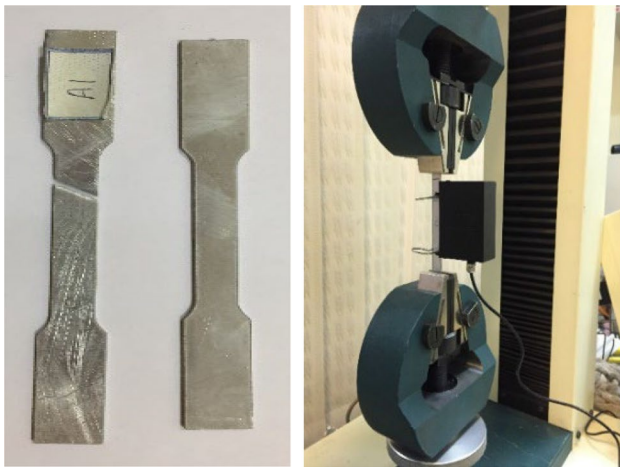
Fig. 4 Tensile test of aluminum

Table 1 Aluminum grade 3000 sample properties

Symbol	Property	Magnitude
ρ	Density $\left(\text{kg}/_{\text{m}^3}\right)$	2770
E	Elastic modulus (GPa)	70
S_{ut}	Tensile strength (MPa)	295
ν	Poisson's ratio	0.33

layers of woven glass fabric. In order to consider the influence of SMA wires embedded between the layers, superelastic SMA wires with a diameter of 0.5 mm were placed in parallel between the third and fourth layers. The volume fraction of fiber in the composite facesheets is about 28%.

2.2 Materials

2.2.1 Aluminum

Figure 4 illustrates the aluminum samples selected for the corrugated core are tested by ASTM B557 standards [41] to exhibit aluminum mechanical properties. Table 1 shows the mechanical properties of aluminum.

2.2.2 Composite facesheet

Composite laminate samples as facesheets were tested according to a) ASTM D3039 standard [42] to demonstrate tensile properties, b) ASTM D5379 standard [43] to demonstrate shear properties, and c) ASTM D6641 standard [44] to demonstrate compressive properties (Fig. 5). The testing results are shown in Table 2 and are used as input properties for numerical analysis.

2.2.3 SMA wires

The SMA wires with the properties given in Table 3 were used to reinforce the facesheets [45].

The parameters involved in the response of smart sandwich panel structures exposed to high strain rate loadings include the influence of SMA presence in reinforcing sandwich structures, the SMA wires' position and numbers, and the pre-strain applied to the SMA wires. To observe the influence of adding SMA wires to structures, three types of samples were made and tested, including a sample without SMA wires (Fig. 6a), a 6-wires SMA sample with three wires in the front facesheet and three wires in the back facesheet (Fig. 6b), and a 12-wires SMA sample with six wires in the front facesheet and 6 wires in the back facesheet (Fig. 6c). To observe the effect of SMA wires position, in the 6-wires sample, the wires are embedded in such a way that one of the wires is exactly situated at the center of the facesheet and the projectile hitting point on the structure; in the 12-wires sample, the wires are embedded in such a way that the central projectile is hitting the sample at an equal distance of 0.25 cm from each adjacent SMA wires, as illustrated and specified by '×' marks in Fig. 6b and c. The central position of impact is also displayed by the '×' mark in Fig. 6. To observe the pre-strain effect, in the 6-wires samples, the SMAs are embedded in composite facesheets in two various forms: 0% pre-strain and 3% tensile pre-strain. All samples were made in $15 \times 15 \text{cm}^2$ dimensions. Definitions of sample codes and parameters are listed in Table 4.

The SMA wires' quantity for each facesheet is written by a number before W; similarly, the number after W corresponds to the pre-strain condition of the wires. Also, GE means facesheets made of glass fiber /epoxy composites without the SMA wires, and SGE means the facesheets with the SMA wires.

2.3 High strain rate test

A high strain rate test was done using an air gun shown in Fig. 7. The air gun generates the required speed and strain rate for the projectile using a pressure vessel. This testing rig is normally employed to test for high and medium strain rate impacts whereby a low mass projectile is propelled using pressurized air in the gun barrel. The speedometer is comprised of a diode emitting a light beam and a light indicator. The projectile, which is of a specific dimension, blocks the light beam, and the duration of blockage is recorded by a sensor. To calculate the projectile speed, the time interval between the two sensors is measured by a digital counter.

Fig. 5 The facesheet laminate samples under (**a**) shear test, (**b**) compression test and (**c**) tensile test

The sample's holder fixed the samples by support to fix the edges from each side by 5 cm. (Fig. 8). The projectile used in the study is a cylindrical object with a semi-spherical head of 21 mm in diameter and 27 gr in weight (Fig. 9). The projectile, which was made of steel was so stiff (rigid), that no deformation occurred during the impact.

The projectile's initial speed in this study is 119 m/s.

3 Finite element modeling

3.1 Software and geometry model

A finite element LS-Dyna R11 commercial FE code was used for the numerical simulation. LS-Dyna is a nonlinear dynamic modeling program that relies on explicit equations to simulate problems. In this study, the geometry is of four parts: an impactor (projectile), an aluminum corrugated

Table 2 Composite laminate properties used as facesheets

Symbol	Property	Magnitude
ρ	Density	1460 (kg/m^3)
E_{11}	Longitudinal Young's modulus	19.84 (GPa)
E_{22}	Transverse Young's modulus	19.84 (GPa)
ν	Poisson's ratio	0.25
G_{12}	Shear modulus	5 (GPa)
X_t	Tensile strength—Longitudinal	369 (MPa)
X_c	Compressive strength—Longitudinal	375 (MPa)
Y_t	Tensile strength—Transverse	369 (MPa)
Y_c	Compressive strength—Transverse	375 (MPa)
S	Shear strength	75.8 (MPa)

Table 4 Samples' code in the present research

Number	Samples code	Number of wires in each facesheet	Wires pre-strain (%)
1	GE-0W0	0	0
2	SGE-3W0	3	0
3	SGE-3W3	3	3
4	SGE-6W0	6	0

core, two composite facesheets at top and bottom of the core, and SMA wires to reinforce composite plates as shown in Fig. 10.

Properties of the rigid body were applied to the impactor. Using the Belytschko-Tsay shell element formula, the aluminum corrugated core is modeled with three integration points in the direction of thickness. The aluminum corrugated core thickness is 0.3 mm, similar to those of the tested samples. The composite facesheets are modeled by shell elements with four integration points in the direction of thickness. The composite plates are 1 mm in thickness, each with four layers. Additionally, to model the SMA wires, a beam element is used with Hughes-Liu with a circular cross section and 0.5 mm in diameter. The dimensions of square-shaped samples are assumed as 15 × 15 cm^2. The height of the aluminum corrugated core is 1.1 cm, whose cross section is shown in Fig. 11.

As shown in Fig. 12, the impactor modeled is a cylindrical object with a semi-spherical head, 3.75 cm in length, a radius of 1.08 cm, and a mass of 27 gr. The place of impact is exactly at the center of the sample.

Table 3 Properties of Shape memory alloy wire [45]

| Symbol	Property	Value
ρ	Density	6500 (kg/m^3)
E^A	Young's modulus—Austenite	55 (GPa)
E^M	Young's modulus—Martensite	46 (GPa)
υ	Poisson's Ratio	0.3
σ^{As}	Stress level at which martensite-to-austenite phase transformation starts	190 (MPa)
σ^{Ms}	Stress level at which austenite-to-martensite phase transformation starts	380 (MPa)
σ^{Af}	Stress level at which martensite-to-austenite phase transformation finishes	120 (MPa)
σ^{Mf}	Stress level at which austenite-to-martensite phase transformation finishes	460 (MPa)
H^{cur}(380MPa)	Recoverable strain	5.6%
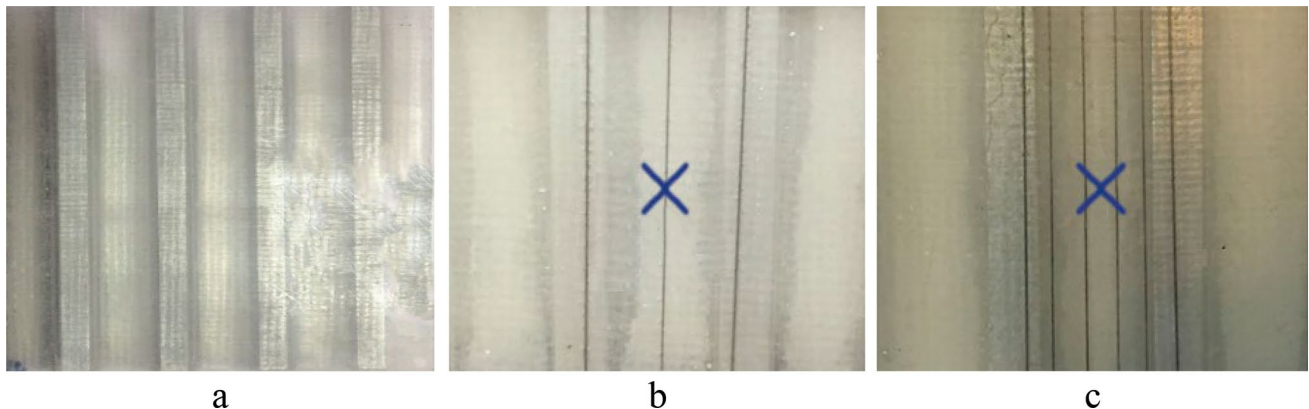
Fig. 6 The samples (**a**) without wire, (**b**) with 6 wires, and (**c**) with 12 wires

Fig. 7 The utilized air gun impact test device

Fig. 8 Sample's holder

Fig. 9 Semi-spherical projectile
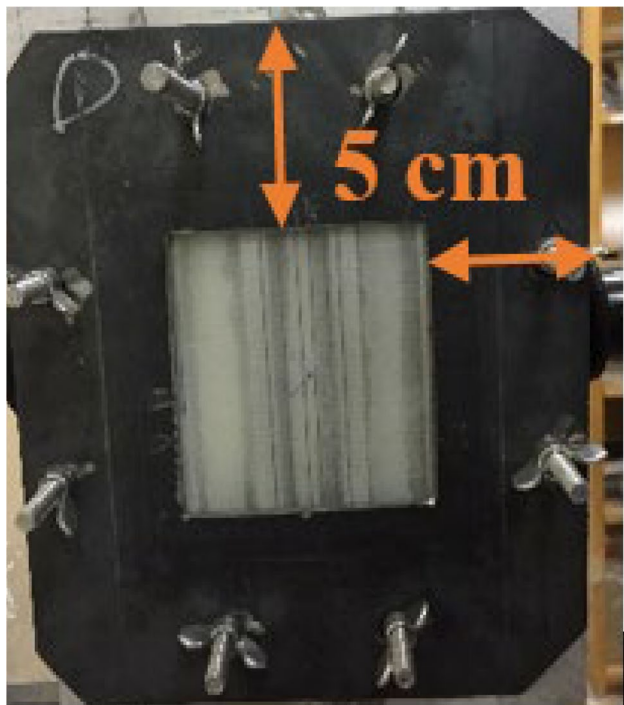
Three models are presented in this study: a sample without SMA wire, a sample with 3 SMA wires for each composite facesheet, and a sample with 6 SMA wires in each composite facesheet (Fig. 13).

In 3 SMA wires-reinforced composite facesheets, the middle wire is exactly at the center of the facesheet under the projectile hitting point. In 6 SMA wires-reinforced composite facesheets, the two-middle adjacent SMA wires are located at 0.25 cm apart from the center of the facesheet and the projectile hitting point. Figure 14b and c illustrates the positions of SMA wires in the samples with 3 SMA wires and 6 SMA wires in each facesheets, respectively.
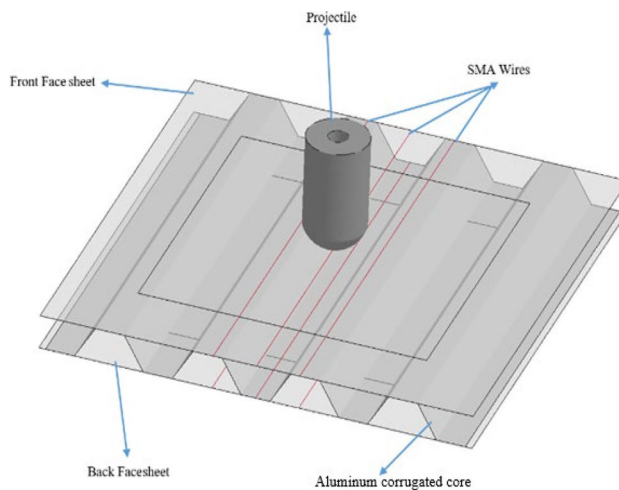

Fig. 10 FEM Geometry for SGE-3W0

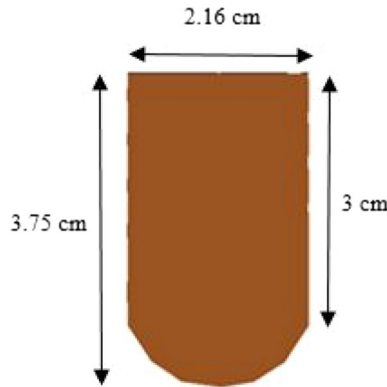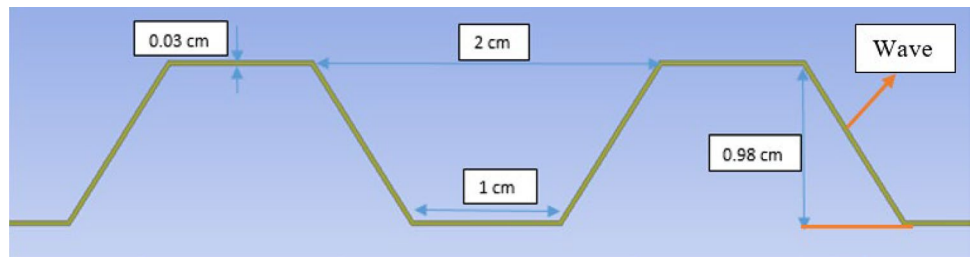**Fig. 11** Core cross-sectional view

Fig. 12 The geometry of the projectile

3.2 Material properties

3.2.1 Composite facesheet

An enhanced composite damage model is employed for composite facesheets. In the elastic area, Hallquist [46] and Wade et al. [47] provided the stress–strain behavior of the material in the longitudinal, transverse, and shear directions.

$$\varepsilon_1 = \frac{1}{E_1}(\sigma_1 - v_{12}\sigma_2) \tag{1}$$

$$\varepsilon_2 = \frac{1}{E_2}(\sigma_2 - v_{21}\sigma_1) \tag{2}$$

$$2\varepsilon_{12} = \frac{1}{G_{12}}\tau_{12} + \alpha\tau_{12}^3 \tag{3}$$

The parameter 'α', in Eq. (3), considers the weighing factor of the nonlinear shear stress. 'α' is normally calibrated by trial
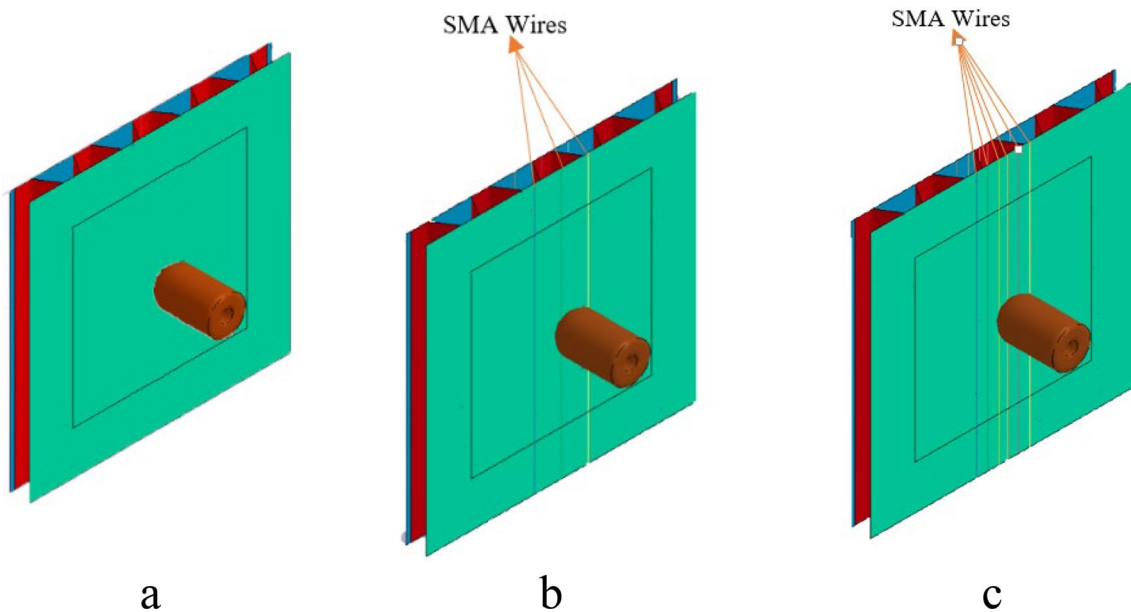

Fig. 13 The geometry of samples and the impactor (**a**) without SMA (**b**) with 3 SMA wires in each facesheet (**c**) with 6 SMA wires in each facesheet
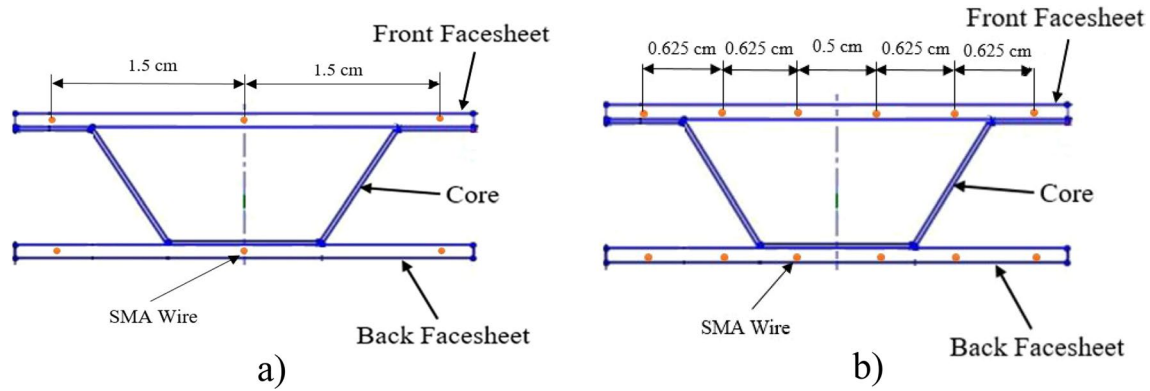
Fig. 14 Schematic view of the SMA's wires location in the samples (**a**) 3 SMA wires in each facesheet and (**b**) 6 SMA wires in each facesheet

and error as it cannot be determined experimentally. In order to specify individual ply failure, as presented in the following Eqs. (4–8), the material model uses the Chang-Chang failure criterion [46, 47] out of the elastic region. Equations. (4–8) show e_t and e_c, which are called the history variables representing tension and compression as failure flags (or indicators.)

For the tensile-axial direction mode where $\sigma_{11} > 0$

$$e_t^2 = \left(\frac{\sigma_{11}}{X_t}\right)^2 + \beta\left(\frac{\sigma_{12}}{S_c}\right)^2 - 1, \quad \begin{array}{l} e_t^2 \geq 0 \Rightarrow \text{failed} \\ e_t^2 < 0 \Rightarrow \text{elastic} \end{array} \quad (4)$$

Upon failure: $E_1 = E_2 = G_{12} = v_{12} = v_{21} = 0$.

In the tensile fiber mode,'β', which is regarded as the shear stress weighing factor, makes it possible for the user to define the influence of shear explicitly.

The Hashin failure criterion is derived for $\beta = 1$, where setting $\beta = 0$, Eq. (4) is reduced to the maximum stress failure criteria.

In case of the compressive-axial direction mode where $\sigma_{11} < 0$

$$e_c^2 = \left(\frac{\sigma_{11}}{X_c}\right)^2 - 1, \quad \begin{array}{l} e_c^2 \geq 0 \Rightarrow \text{failed} \\ e_c^2 < 0 \Rightarrow \text{elastic} \end{array} \quad (5)$$

Upon failure: $E_1 = v_{12} = v_{21} = 0$.

For the tensile-transverse direction mode where $\sigma_{22} > 0$

$$e_t^2 = \left(\frac{\sigma_{22}}{Y_t}\right)^2 + \beta\left(\frac{\sigma_{12}}{S_c}\right)^2 - 1, \quad \begin{array}{l} e_t^2 \geq 0 \Rightarrow \text{failed} \\ e_t^2 < 0 \Rightarrow \text{elastic} \end{array} \quad (6)$$

For the compressive-transverse direction mode where $\sigma_{22} < 0$

$$e_c^2 = \left(\frac{\sigma_{22}}{Y_c}\right)^2 - 1, \quad \begin{array}{l} e_c^2 \geq 0 \Rightarrow \text{failed} \\ e_c^2 < 0 \Rightarrow \text{elastic} \end{array} \quad (7)$$

For the matrix failure criterion

$$e_t^2 = \left(\frac{\sigma_{12}}{S_c}\right)^2 - 1 \quad (8)$$

where S_c is the shear strength, X_t and X_c are the tension and compression strength in longitudinal direction, respectively. Similarly, Y_t and Y_c are the tension and compression strength in transverse direction, respectively. The mechanical test results (Table 2) will be used for input parameters.

In order to define failure, the Chang-Chang model [46, 47] is used. This material model shows that when a failure occurs in all the composite layers (through-thickness integration points), the element is deleted. For bricks, once the integration point has met the failure criteria, the element is removed [48].

According to the results presented in the references [49], the strain rate has no effect on Young's modulus, and by increasing the strain rate to $1000s^{-1}$, the ultimate strength has increased 50% more than its value at the quasi-static strain rate ($0.001s^{-1}$) in glass/epoxy composite laminates. In the present paper, the strain rate is equal to $370s^{-1}$. According to the results presented in the references [49] and by interpolating between the ultimate stresses at $0.001s^{-1}$ and $1000s^{-1}$ strain rates, the ultimate strengths presented in Table 2 are approximately changed to 437 MPa, 444 MPa, and 90 MPa for $X_t(Y_t), X_c(Y_c)$ and S_c, respectively.

3.2.2 Aluminum corrugated core sheet

The aluminum corrugated core is modeled by Piecewise Linear Plasticity. Elastoplastic properties for this material are addressed by the definition presented by the stress–strain curve. Failure properties are defined by effective plastic strain (EPS). Table 1, presents the defined mechanical parameters for aluminum.

The Cowper–Symonds model [48] is used to include the effect of the strain rate:

$$1 + \left(\frac{\dot{\epsilon}}{C}\right)^{1/P} \qquad (9)$$

where $\dot{\epsilon}$ is the strain rate, for aluminum alloys, the constant coefficients P and C are 4 and 6500 1/s, respectively, [49].

3.2.3 Shape memory alloys

In order to define SMA properties, the shape memory material model is employed. This material defines the superelastic behaviors of SMA materials, whereby the material can tolerate huge transformations due to loading and restoring the original case due to unloading. The required parameters to define SMA include density, elastic modulus in the austenite phase, Poisson's ratio, initial austenite stress, final austenite stress, initial martensite stress, and elastic modulus in the martensite phase. Table 3 shows the parameters. Also, according to the results presented in reference [50, 51], increasing the strain rate leads to increase the stress level at the plateau area in the loading state (phase transformation from austenite to martensite). On the other hand, by increasing the strain rate in the unloading state (phase transformation from martensite to austenite), the stress level remains constant. The results presented in reference [50, 51] show that by increasing the strain rate from $0.001 S^{-1}$ in quasi-static test, up to $1200 S^{-1}$ in dynamic test, the starting and the final value for the forward phase transformation (σ^{Ms} and σ^{Mf}, respectively) will increase about 100 MPa. According to the results in reference [50, 51], by interpolating between the stresses value, the σ^{Ms} and σ^{Mf} which were presented in Table 3, are increased about 30 MPa and calculated to be about 410 and 490 MPa, respectively. Before doing the dynamic analysis, each of the SMA wires in pre-strained samples was stretched by suppose 1.5% of its original length, which equals 2.25 mm from both sides of the wire (the case of 3% pre-strain for each wire).

3.2.4 Rigid body projectile

The experiment showed that the impact process did not cause any deformation to the projectile, so the projectile was modeled as a rigid material that is stiff enough to resist any deformation while impact on sandwich panel.

Table 5 Rigid body properties used as projectile

Symbol	Property	Magnitude
ρ	Density	7850 (kg/m^3)
E	Young's modulus	200 (GPa)
ν	Poisson's ratio	0.3

This material model is allowed to directly define the internal properties and initial velocities for the projectile, and it will calculate the override data from the material property definition. The sliding interface parameters depend on Young's modulus and Poisson's ratio, when there is a contact definition involving the rigid body. [46] The projectile material properties are shown in Table 5.

3.3 Mesh details

Each composite facesheets layer was meshed using 2416 ELFORM = 2 Belytschko-Tsay shell elements. The impactor was meshed using 5105 selective reduced integrated rigid elements (ELFORM = 16). The aluminum core was meshed using 2416 ELFORM = 2 Belytschko-Tsay shell elements. Each SMA wire was meshed using 48 ELFORM = 1 Hughes-Liu beam elements.

3.4 Contact definition

LS DYNA's "Contact Automatic Surface to Surface" formulation was used to model the contact interaction between the impactor, composite facesheets, and aluminum corrugated core. Once an external surface of a body comes in contact with the external surface of another body, the Automatic Surface to Surface algorithm can establish contact. Automatic Surface to Surface is considered the most general type of contact used as LS-DYNA automatically searches all the external surfaces in a model to determine the occurrence of penetration.

Using an epoxy adhesive, the laminated composite facesheets are attached to the corrugated core. Wentao et al. [52] established via the experimental results that there is no clear observation of debonding failure among the corrugated core and the facesheets during the impact tests. Therefore, LS DYNA's "Contact Tied Surface to Surface Offset" formulation was used to model the contact interaction between the aluminum core and each composite facesheet. Gluing contact surface to target surface may be of interest when the meshes are not matching. The master node can deform and the slave node will follow. In this contact model, the debonding and delamination between the master and slave bodies are not taken into consideration. Instead, the contact is assumed to be perfectly tied. Therefore, in the contact areas, the surfaces of the two bodies that are joined together would behave as a single entity with distinct properties.

Modeling of contact interaction between the SMA and each composite facesheets was done by LS DYNA's "Contact Tied Node to Surface Offset" formulation.

The "Contact Automatic Node to Surface" connection model is used to make the connection between the impactor
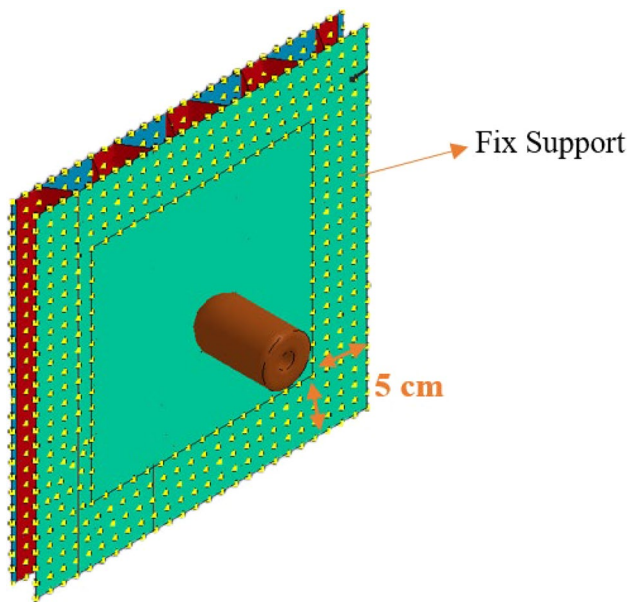
Fig. 15 Boundary Conditions-Fixed supports

and the SMA wires. In this type of connection, each slave node is checked for penetration through the master surface.

3.5 Initial and boundary conditions

The impactor exactly hits the center of the body vertically at the speed of 119 m/s. Considering the boundary conditions and fixtures in the air gun testing machine, the four sides of composite facesheets are assumed as fixed (Fig. 15). As mentioned earlier, before dynamic analysis, each SMA wires was stretched by certain percentage calculated, according to the initial pre-strain conditioned of the SMA wires. In LS-Dyna FE code, the prescribed motion set was used to implement dynamic relaxation conditions for stretching. Dynamic relaxation is applied during the initial phase of the solution to determine the initial stress and displacement field before commencing the analysis. [48]

3.6 Time setup

The time step for outputting the history data was set to 9.00e-4s. The time frame is selected in a manner enabling the impactor to completely penetrate the body and extract from the opposite side of the body. This statement suggests that once the projectile exits a structure, its kinetic energy decreases and eventually converges to zero. As a result, the analysis of the projectile's motion after this point may not be necessary.

3.7 Mesh sensitivity

In FE models, the mesh size has a profound effect on the results. As the mesh size reduces and the number of elements increases, the solution time is subsequently increased. The mesh sensitivity analysis was carried out to arrive the optimal size of the elements. To do so, the meshes need to become very small, so that the results of the two types of samples do not substantially differ. In the samples, meshes are reduced by halves (medium size) and quarters (fine size), and the results are compared with those of the initial meshing (coarse size).

As the number of elements gradually increases, more accurate numerical responses are obtained, and convergence is seen in the results. Three forms of meshing with different element densities were examined, and after reviewing the results, the samples with the medium meshing size were selected. Convergence analysis is based on the residual speed parameters of the projectile.

According to Table 6, in medium and fine meshing as compared with the coarse meshing, the results were close to each other. A comparison of the numerical and experimental solutions to validate the results based on residual speed indicates that there is only about a 1% difference between the results of samples with medium mesh size and fine mesh size. Hence in this study, the medium mesh size was used. Also, Fig. 16 shows the model without SMA wires with different mesh sizes.

Table 6 Mesh convergence of GE-0W0 sample

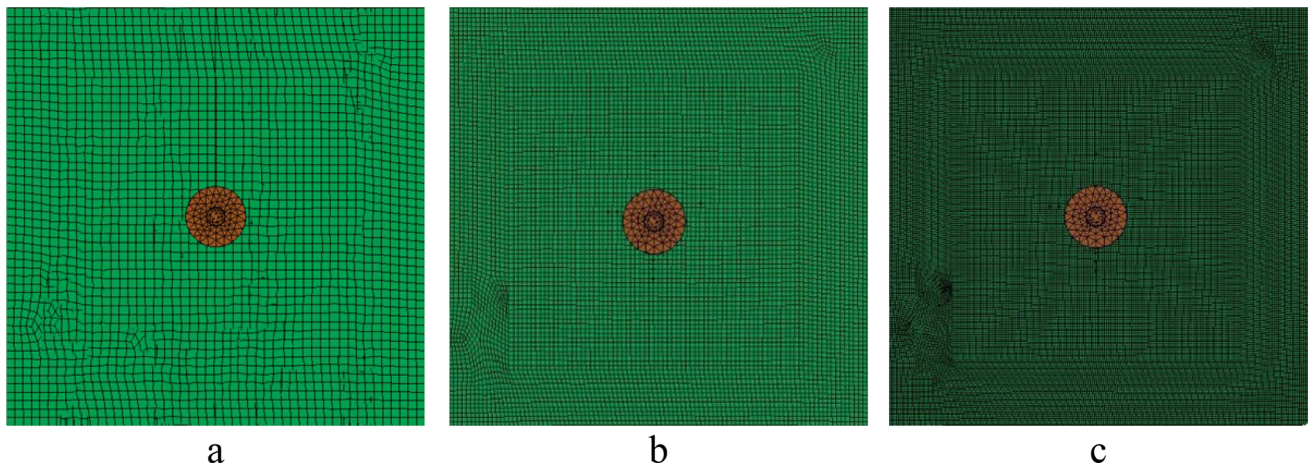| Mesh Size	Total Elements	Total Nodes	Initial Speed (m/s)	Residual Speed (m/s)	Discrepancy with medium mesh size (%)	CPU run time (min)
Coarse	9992	10,341	119	66.2	4.8	15
Medium	39,968	40,663	119	69.5	–	93
Fine	159,872	161,259	119	70.2	1	182

Fig. 16 Models with different mesh sizes (**a**) Coarse size (**b**) Medium size (**c**) Fine size

3.8 Modeling strategy

A flowchart (Fig. 17) is provided to give a concise overview of how the impact on the sandwich panel was considered and solved in LS-Dyna. The initial step involves importing the necessary components, including the geometry and boundary conditions. If a pre-strain is required, a prescribed condition is set accordingly. Once the initial conditions are established, the analysis is started.

The solution progresses until the projectile makes contact with the different parts of the structure. Once contact is established between the impactor and each individual part, the failure criteria of the composite facesheets and the core are evaluated. If the failure criteria are met, the elements are removed, and the impactor continues to pass through the bodies.

The SMA wires are stretched and undergo phase transformation when the impactor is collided with them. Once the impactor is passed through the structure, the check for convergence is conducted and the analysis process is ended.

4 Results and discussion

The limited speed and the absorbed energy by the sandwich panels with the SMA wires were calculated by Eqs. (10) and (11) and compared to the sample with no SMA wires in this study. In this regard, the residual speed of the projectile is calculated. Then, the limited speed and the absorbed energy

were obtained by the experimental results. The limited speed is the minimum required speed of the projectile in order to completely penetrate the body, which is calculated by Eq. (10) [53]. After calculating the limited speed, the absorbed energy is achieved via Eq. (11) [53].

$$V_l = \sqrt{V_i^2 - V_r^2} \qquad (10)$$

$$E_{abs} = \frac{1}{2}M_p V_l^2 \qquad (11)$$

In Eq. (10), V_l, V_i, and V_r associated with the limited, initial, and residual speeds, respectively. In Eq. (11), E_{abs} and M_p are the absorbed energy and the mass of the projectile, respectively.

Moreover, the damage pattern and damage areas of the composite facesheets are examined.

To assess the amount of energy absorbed by the composite facesheets, the damaged area comparison between the front and back (rear) facesheets to the whole surface of the sample might be an adequate criterion. The greater the damaged area, the more energy is absorbed and, therefore the greater the impact resistance.

4.1 High-speed test on GE-0W0 sample

In the first step, the sample in the absence of the SMA wire which is shown in Fig. 6a has been tested. Figure 13a shows the numerical model of the sample. Equation (10) is used to calculate the residual speed and the limited speed,

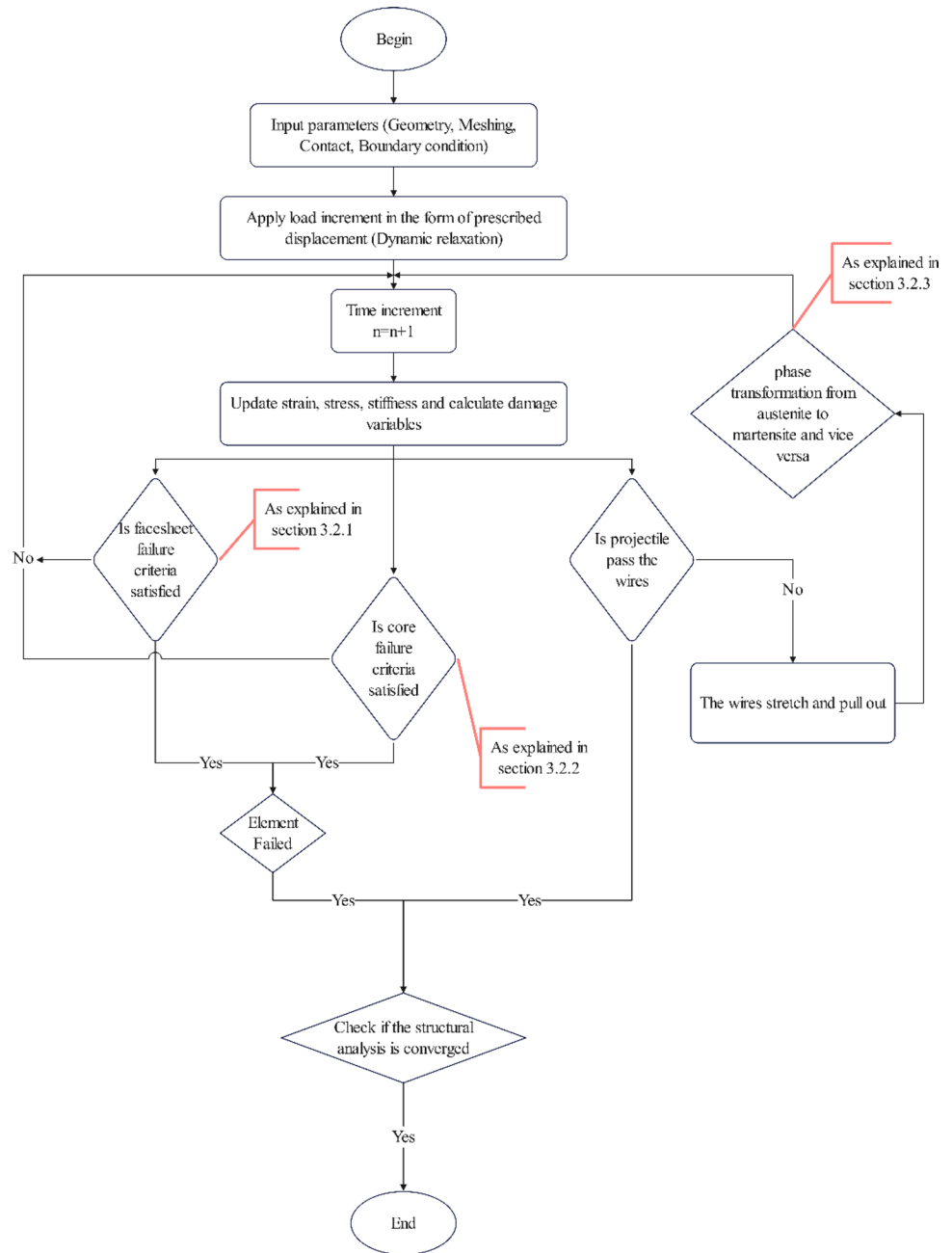**Fig. 17** Flowchart for FE simulation using LS-DYNA

Table 7 Residual speed, limited speed, and absorbed energy for GE-0W0

	Experimental	Numerical	Discrepancy (%)
V_r (m/s)	74	69.5	6.1
V_1 (m/s)	93.19	96.6	3.7
E_{abs} (J)	117.247	125.97	7.4

then to calculate the absorbed energy for the GE-0W0 sample, Eq. (11) is applied. The numerical and experimental results are presented in Table 7. Even in Table 7, the discrepancy between the experimental and the numerical results are also presented. The discrepancy is due to the experimental results which are affected by the instrumental and random errors; the numerical methods are affected by the physical model selected and the parameters belonging to it; on the other hand, in the present study, the shell elements were used to model the sandwich panel, and due to this assumption discrepancy is also occurred.
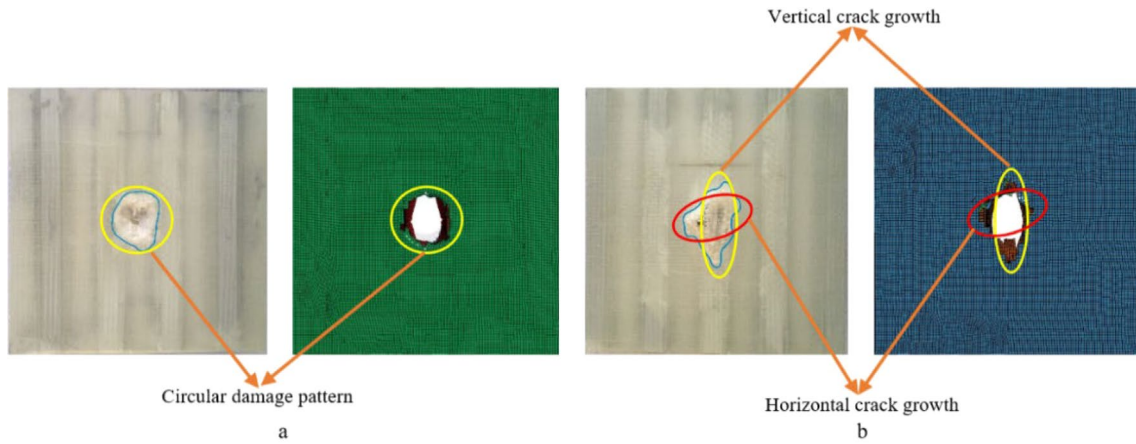
Fig. 18 Damage area of composite facesheet in GE-0W0 sample obtained experimentally (left photograph) and numerically (right photograph) (**a**) front view (**b**) back view

Table 8 Damage area of GE-0W0

	Experimental (cm^2)	Numerical (cm^2)	Discrepancy (%)
Front side	7.86	7.76	1.3
Back side	8.53	9.36	8.86

Table 9 Residual and limited speed, and absorbed energy for SGE-3W0

	Experimental	Numerical	Discrepancy (%)
V_r (m/s)	68	66.3	2.5
V_l (m/s)	97.66	98.8	1.17
E_{abs} (J)	128.749	131.83	2.4

of GE_0W0 obtained by the numerical and the experimental methods after the impact. Moreover, Table 8 presents the damaged areas caused by high-speed test on each surface. It could be concluded that the damaged area on the back side is larger than the front side and more energy is absorbed on the back side because of the contact core and the back facesheet. The damaged area is almost 8.5% greater on the back facesheet. On the front face the damaged area is circular, and the damage propagation on the back side is bidirectional.

4.2 High-speed test on SGE-3W0 sample

Figures 6b and 13b demonstrate the 3 SMA wires facesheets sandwich sample and the numerical model, respectively. The residual and limited speeds, and the absorbed energy for the

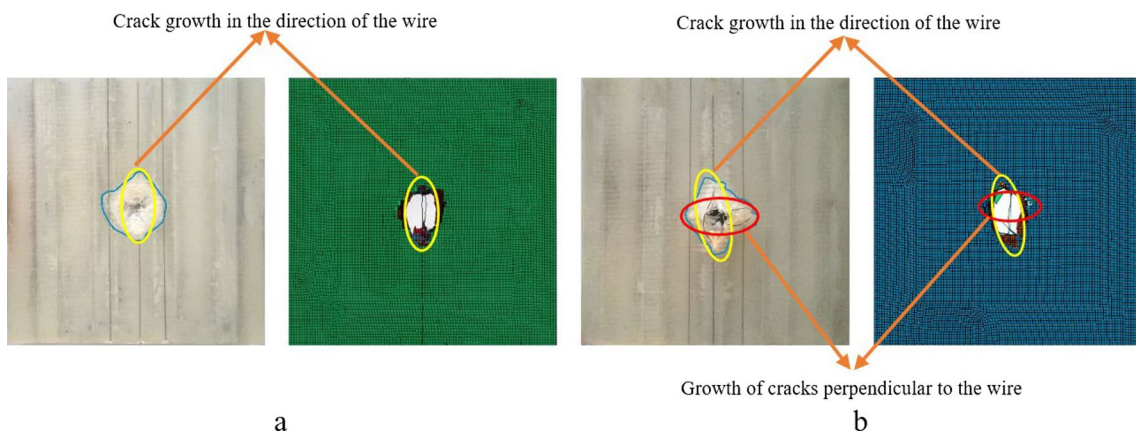Figure 18 shows the front and back damaged surfaces

Fig. 19 Damage area of composite facesheet in SGE-3W0 sample obtained experimentally (left photograph) and numerically (right photograph) (**a**) front view (**b**) back view

Table 10 Damage Area of SGE-3W0

	Experimental (cm^2)	Numerical (cm^2)	Discrepancy (%)
Front side	9.3	9.21	0.96
Back side	9.86	9.26	6.1

Table 12 Damage area of SGE-3W3

	Experimental (cm^2)	Numerical (cm^2)	Discrepancy (%)
Front side	9.4	9.5	1.05
Back side	9.7	9.3	4.1

Table 11 Residual and limited speeds, and absorbed energy for SGE-3W3

	Experimental	Numerical	Discrepancy (%)
$V_r \left(\frac{m}{s}\right)$	60	57	5
$V_l \left(\frac{m}{s}\right)$	102.77	104.46	1.6
E_{abs} (J)	142.574	147.312	3.3

SGE-3W0 sample are calculated by Eqs. (10) and (11) and are presented in Table 9.

Figure 19 shows the front and back facesheets of SGE-3W0 for the experimental and the numerical solutions after the impact. Moreover, Table 10 presents the damaged areas caused by high-speed test on each surface. Results revealed that by including the SMA wires in a sample, about 13% energy absorption of the sandwich panel is increased. Also, adding SMA wires to the facesheets causes larger damaged areas on the front and back surfaces; whence, the greater energy was absorbed by panels. The damaged areas on the front and back surfaces of the sandwich panel at the presence of SMA wires increased by 18 and 16 percent, respectively, when compared to the sample without SMA wires. Furthermore, the direction of damage propagation in the front facesheet is in the direction of the SMA wires. The direction of damage propagation in the back facesheet is in the direction and the vertical direction of the SMA wires. That is why the back facesheet damage area was about 6% greater than the front facesheet.

4.3 High-speed test on SGE-3W3 sample

Table 11 demonstrates the residual and limit speeds, and absorbed energy that are obtained by Eqs. (10) and (11) for the experimental and numerical study of the high-speed test on the SGE-3W3 sample, that is, the SMA wires are pre-strained by 3%.

Figure 20 shows the front and the back damaged surfaces of SGE-3W3 for the numerical model and the experimental sample after the impact. Moreover, Table 12 presents the damaged areas caused by high-speed impact on each surface. Results indicated that the pre-strain of the SMA wires caused an increase of about 21.5% greater energy absorption as compared to GE-0W0 and about 11% greater energy absorption as compared to SGE-3W0. There is an increase in the damaged area on the front surface and a reduction in the damaged area on the back surface measured against the sample without pre-strain SMA wires. Approximately
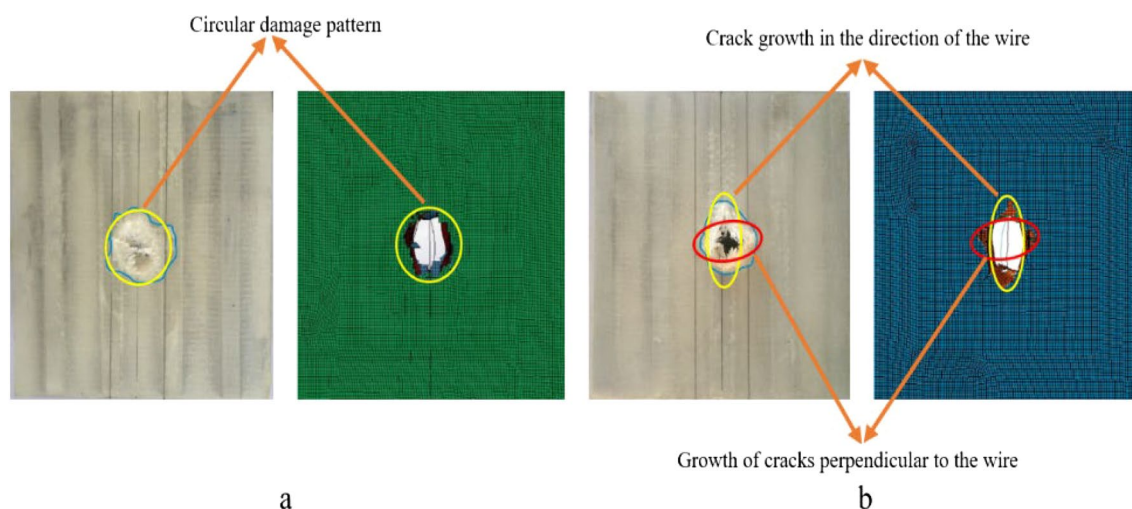

Fig. 20 Damage Area of composite facesheet in SGE-3W3 sample obtained experimentally (left photograph) and numerically (right photograph) (**a**) front view and (**b**) back view

Table 13 Residual speed, limited speed, and absorbed energy for SGE-6W0

	Experimental	Numerical	Discrepancy (%)
$V_r\left(\frac{m}{s}\right)$	71	69.3	2.4
$V_l\left(\frac{m}{s}\right)$	95.5	96.74	1.3
$E_{abs}(J)$	123.12	126.34	2.6

20% increase in the front facesheet and 14% increase in the back facesheet damaged area occurred when compared to GE-0W0. The damaged area on the front surface is approximately circular and the direction of the damage propagation is also in both the direction and vertical direction of the SMA wires. It shows that the pre-strain of the SMA wires would change the behavior of the failure and energy absorption of the sample, since the projectile hit the pre-strained wire at the center and the adjacent wires also affect the energy absorption in the front facesheet compare to the back facesheet.

4.4 High-speed test on SGE-6W0 sample

Figure 6c shows the 6 SMA wires facesheets sandwich sample. Figure 13c shows the numerical model of the sample. Equation (10) is used to calculate the residual and limited speeds, and Eq. (11) is applied to calculate absorbed energy for the SGE-6W0 sample. Table 13 lists the numerical and experimental results.

Figure 21 shows the front and back sides of SGE-6W0 for the numerical and experimental investigation after the high-speed test. Moreover, Table 14 presents the damaged areas caused by high-speed impact on each surface. Results

Table 14 Damage area of SGE-6W0

	Experimental (cm^2)	Numerical (cm^2)	Discrepancy (%)
Front Side	8.57	9.2	6.8
Back Side	9.1	9.8	7.1

Table 15 Mass of samples

Sample	GE-0W0	SGE-3W0	SGE-3W3	SGE-6W0
Mass (gr)	103.02	104.16	104.17	105.32

demonstrated that about a 5% increase in absorbed energy was achieved by 6 SMA wires facesheets in the sandwich panel as compared to GE-0W0. It should be noticed that the hitting point is in between the SMA wires and not on the SMA wire. The damaged area increases on the front side as well as on the back side when compared to GE-0W0; therefore, adding the SMA wires caused the sandwich panel to absorb more energy. The front and back facesheets damaged areas are becoming larger by 9% and 6.8%, respectively, when compared to GE-0W0 sample. Damage propagation is in the direction of SMA wires in the form of a long oval on the front and back sides.

Due to slight difference in the dimensions and the weights of the samples in the fabrication process, the specific absorbed energy (SAE), which is the result of dividing the absorbed energy by the mass of each sample, has been calculated by Eq. (12).

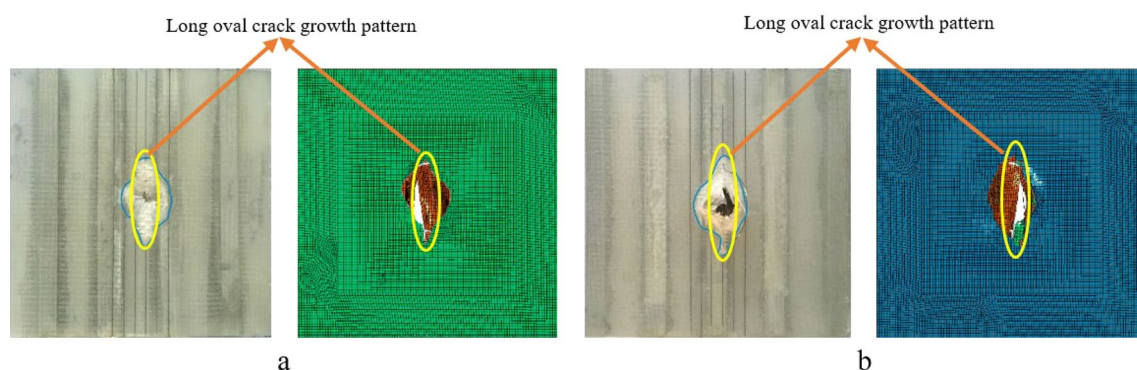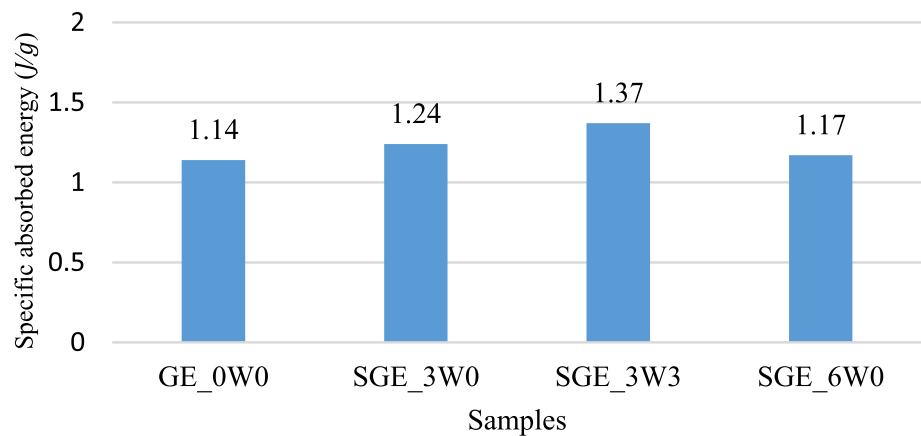$$\text{SAE} = \frac{E_{abs}}{m}\left(\frac{J}{gr}\right) \qquad (12)$$

Fig. 21 Damage area of composite facesheet in SGE-6W0 sample obtained experimentally (left photograph) and numerically (right photograph) (**a**) front view and (**b**) back view

Fig. 22 Specific absorbed energy – SAE (*J/g*)

Table 16 Total absorbed energy for all samples in the present work

Sample	Experimental total absorbed energy (*J*)	Numerical total absorbed energy (*J*)	% increase in Absorbed Energy (Experiment)
GE-0W0	117.247	125.97	0
SGE-3W0	128.749	131.83	9.8
SGE-3W3	142.574	147.312	21.6
SGE-6W0	123.12	126.34	5

In Eq. (12), E_{abs} refers to the absorbed energy that was calculated by Eq. (11) and '*m*' refers to the mass of samples.

The mass of each sample is presented in Table 15. Figure 22 shows the SAE obtained by the experiments. Considering the mass of each sample, the SAE increased by embedding SMA wires in the sandwich panel. Furthermore, applying the pre-strain to the wires caused the SAE increases. The results show that the shape memory wires placed at the hitting point work to the advantage of more specific energy absorption.

In the research made by Ref. [38], the influence of SMA wires on the high-speed impact resistance of smart fiber metal laminate (FML) was investigated. The results in reference [38] showed that embedding SMA wires between composite layers in FML increases the energy absorption of the structure. So, the samples with 2, 4, and 8 wires in the Ref. [38], absorbed more energy than the samples without wires. However, increasing the volume fraction of SMA wires (no. of SMA wires), decreases the absorbed energy due to the discontinuity in mechanical properties of the samples [38]. The energy absorption was increased following the application of pre-strain to the SMA wires. According to the results in Ref. [38], by applying 4% pre-strain to the SMA wires in the sample with 4 wires, the absorbed energy was increased about 10.2% compared with the sample includes 4 wires without pre-strain. In the present research, by increasing the pre-strain to 3% in the SGE-3W3 sandwich samples,

the absorbed energy is increased by almost 10.7% compared with the SGE-3W0 sample. As shown in Table 16, it is determined that placing SMA wires in the structures can improve the high-speed impact resistance. Pre-straining the SMA wires in sandwich panel is dominant factor than increasing the number of SMA wires. Also, there is a good agreement between the experimental and the numerical results.

4.5 Damage morphology

Based on the results of the high-speed impact tests performed on sandwich panel samples with corrugated cores, including the facesheets at the presence of the SMA wires and without the presence of the SMA-wires, the failure mechanisms comprised of numerous stages:

The first stage is the moment the projectile strikes the front composite facesheet at initial speed. At this stage, a portion of the projectile energy is absorbed by the front facesheet, and failure is seen in the matrix and fibers. In samples with 3 SMA wires facesheets, after the projectile collides with the middle wire, a portion of the projectile energy is absorbed by the SMA wires. The absorption of energy continues until the projectile pulls out the SMA wire. It has been observed that in these samples, the projectile deviated slightly after passing through the middle SMA wire. In 6 SMA wires facesheets samples, the two SMA wires situated near the impact point absorb a part of the projectile energy. In all samples with the SMA wires, due to the collision of the projectile with the SMA wires, the wires are stretched and then, the projectile gets past the wires, and the stretch is partially recovered.

In the second stage, the projectile penetrates the front composite facesheet and reaches the aluminum corrugated core. In this stage, a significant amount of energy is absorbed by the aluminum corrugated core. As the penetration process continues, the stress reaches the ultimate stress in the aluminum that causes the core penetration and petaling. At this stage, due to the deformation of the core, the adhesive bond

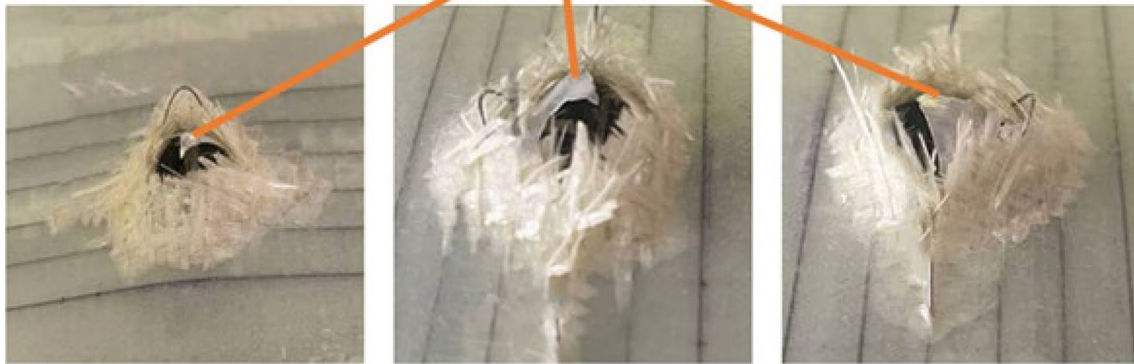The petal fracture of the core caused the failure of the composite back facesheet

Fig. 23 Influence of the core crack on the rear facesheet failure

between the core and the back composite facesheet is failed in some locations around the impact point (it was visible by color changed in the matrix around the impact point). Petal cracks in the core also caused fracture in the back composite facesheet. In the study of Ref. [54], the effect of core shape on the impact performance of sandwich panels at different impact velocities, including high-speed impact was studied numerically. In Ref. [54], five types of cores were studied: Kagome-3D, pyramidal, corrugated, hexagonal honeycomb, and tetrahedral. They simulated the impact at three different velocities: 10, 40, and 200 m/s. The results show that at the low-speed and high-speed of the projectile, the corrugated core sandwich panel absorbed more energy than other sandwich panel core configurations. Figure 23 demonstrates the

influence of the core crack on the back facesheet rupture in the SGE-6W0 sample. Due to this type of fracture behavior in corrugated core, the sandwich panels usually absorb more energy.

In the third stage, the projectile leaves the sample after passing through the core and ruptures the matrix and fibers of the back facesheet. At this stage, the projectile loses energy again due to the collision with the SMA wires, and as in the first stage, the projectile causes a stretch in the SMA wires. After the completion of the impact process and complete passage of the projectile through the SMA wires and facesheet, part of this stretch is returned.

Fig. 24 Absorbed energy history
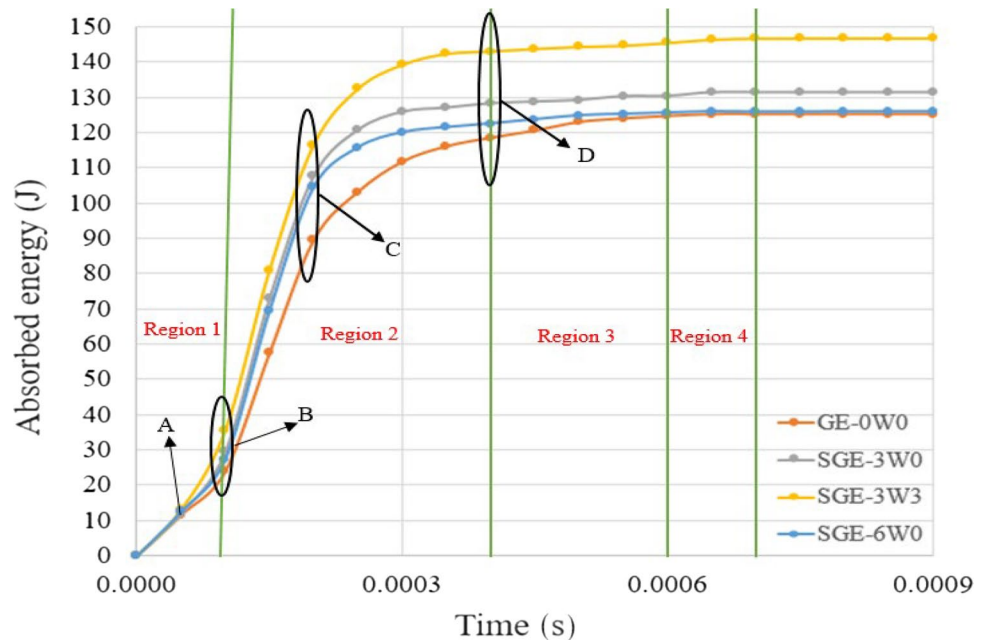
4.6 Absorbed energy history

The absorbed energy-time graph obtained through numerical solutions is shown in Fig. 24 indicates that: Region 1, initially, all absorbed energy history graphs show a linear upward increase for all samples up to Point A due to the impact of the projectile on the front composite facesheets. Then, the steepness of the absorbed energy-time graph is increased from Point A to point B due to the stretching of the SMA wires in the samples with the SMA wires. The sample SGE-3W3 deviated more due to pre-strain of the SMA wires.

At Region 2, the projectile hits the aluminum corrugated core which accounts for much of the absorbed energy by the sample (point B to point C). The change in steepness in this region is due to achieved stiffness of the whole structure due to the presence of the SMA wires. At this region, in addition to the absorption of energy by the aluminum core, some energy is absorbed by the back composite facesheet and the bonding with the aluminum core during the nonlinear region of the graph (Point C to point D).

At Region 3, the projectile is passing through the facesheet on back showing the highest amount of the absorption of energy by the friction of the components of the sandwich panel, the projectile, along with the SMA wires (point D onward).

In Region 4, finally, the structure solely absorbs energy from the SMA wires. As shown in Fig. 24, the amount of energy absorption is increased during the four regions by adding the SMA wires and pre-strain to the SMA wires in the samples.

Additionally, placing the SMA wires at the hitting point of the projectile impact leads to an increase in the steepness of the absorbed energy history at region 1 and region 3. On the other hand, applying pre-strain to shape memory wires also causes an increase in the steepness of the absorbed energy-time graph at regions 1 and 3 and specifically at the end of the region 2.
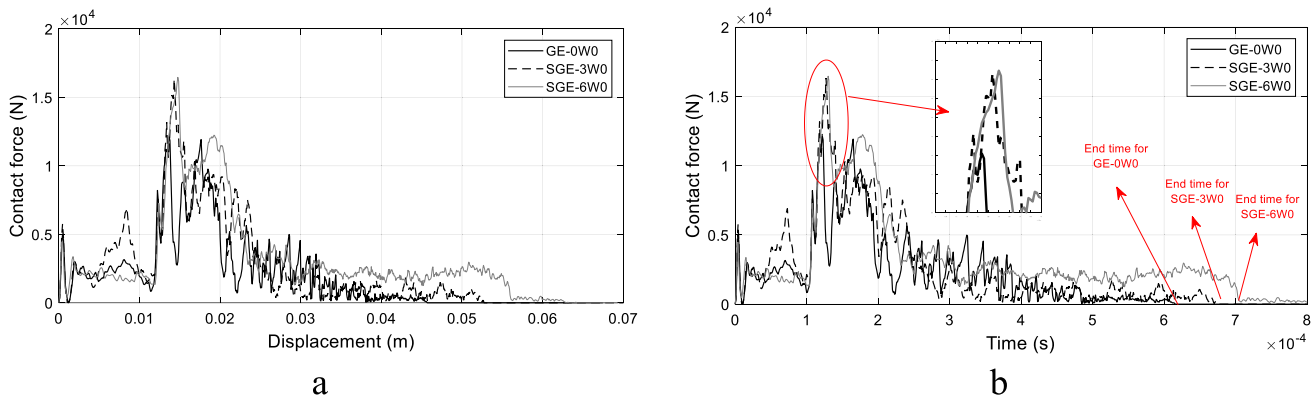

Fig. 25 (**a**) contact force–displacement curves, (**b**) contact force history for GE-0W0, SGE-3W0, and SGE-6W0 samples
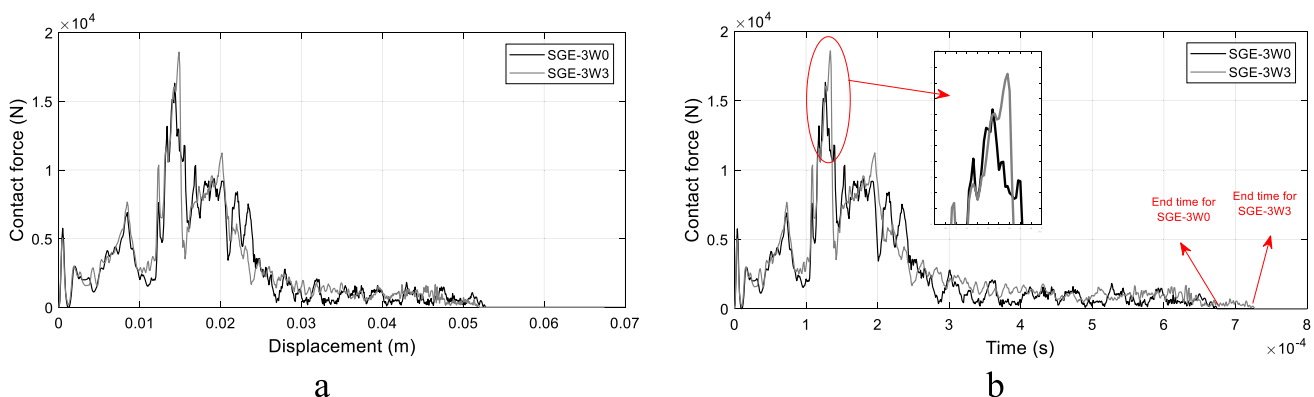

Fig. 26 (**a**) contact force–displacement curves, (**b**) contact force history for GE-3W0 and SGE-3W3 samples

4.7 Contact force history

Figures 25 and 26 show the a) contact force versus displacement curves and b) contact force history for all the sandwich samples during the impact time resulting from the numerical analysis, respectively. Figure 25 shows the effect of placement of SMA wires, its quantity and its location, and Fig. 26 shows the pre-strain effect of SMA wires. The results revealed that embedding the shape memory wires with 0% pre-strain in the composite facesheets (Fig. 23a) increases the contact force. The maximum contact force increases from 12.1 kN for GE-0W0 to 16.2 kN and 16.3 kN for SGE-6W0 and SGE-3W0, respectively. These results showed that placing the SMA wires precisely at the hitting point exhibits an increase of about 34.8% in maximum contact force and is more efficient as compared to SGE-6W0, where there are 6 SMA wires in the facesheet and are away from the impact point (33.8%). Due to applying the pre-strain to the shape memory wires, the maximum contact force increased from 16.3 kN for SGE-3W0 sample to 18.6 kN for SGE-3W3 samples (Fig. 24a), that is, a 53.8% increase as compared to GE-0W0 sample and 14% increase as compared to SGE-3W0 sample.

Considering the results shown in Figs. 25b and 26b, by embedding the SMA wires without pre-strain exactly at the hit point, the time of impact duration increased from 617 μs for.

GE-0W0 to 674 μs for SGE-3W0 samples (increased by about 9%). The time needed for the projectile to pass through the sandwich panel increased from 674 μs for SGE-3W0 to 708 μs for the SGE-6W0 sample; that is, increased by 5%. Due to applying the pre-strain to shape memory wires, the time required for the full penetration increased from 674 μs for SGE-3W0 to 727 μs for SGE-3W3 samples (increased by about 8%). These results also showed that the sample in which more SMA wires are placed and the middle SMA wires are located at a distance from the impact point has a greater advantage in delaying the impact time compared to the sample in which the SMA wires are exactly located at the impact point and with less number of SMA wires, hence the shocking effect is reduced. This is due to enhancement of stiffness of the sandwich sample by placement of the SMA wires in the composite facesheets. But, the pre-straining the SMA wires, presented dominant effect on the impact behavior of the samples, it means that the impact duration is increased by about 18% compared to.

GE-0W0 sample. The other advantage is by considering the results shown in Fig. 25b and 26b. As the SMA wires are added to the samples, the peak point on contact force history moves to the right for all the SMA embedded facesheets samples, means SGE-3W0 and SGE-6W0 and SGE-3W3, but again the effect of pre-strain of the SMA wires are more predominant. Therefore, adding the SMA

Table 17 Residual and limited speeds, and absorbed energy for SGE-3W6, and SGE-3W8 samples

Numerical Results	SGE-3W6	SGE-3W8
$V_r\ (^m/_s)$	54.9	53.5
$V_l\ (^m/_s)$	105.6	106.3
E_{abs} (J)	150.5	152.5

wires to the samples increases the impact duration as well as the time to reach the maximum contact force and hence decreases the impact shocking effect to the structures.

The area under the curves obtained numerically presented in 25a and 26a was calculated and it was found to be approximately same as the numerical results obtained by FE code based on initial and residual velocities of the projectile presented in Table 16.

4.8 The effect of pre-strain on the SMA wire's energy absorption

To examine the effect of pre-strain on the SMA wires energy absorption, the SGE-3W6 and SGE-3W8 samples, to be precise, the 3 SMA wires with 6%, 3 SMA wires with 8% pre-strain applied to the SMA wires samples, respectively, are investigated using LS-DYNA FE commercial code, along with the other 3 SMA wires samples, namely, SGE-3W0 and SGE-3W3, which the information given in pervious sections. The residual and limited speeds, and absorbed energy for the SGE-3W6, and SGE-3W8 samples are listed in Table 17.

Owing to the numerical results, by adding pre-strain to SMA wires, the absorbed energy increased from 131.83 J for SGE-3W0 to 147.312 J, 150.5 J, and 152.5 J for SGE-3W3, SGE-3W6 and SGE-3W8 samples, respectively.

Figure 27 shows the energy absorbed history by the SMA wires for samples with 3 SMA wires with and without pre-strain in each facesheets. The results showed that the energy absorbed by the SMA wires increases by applying more pre-strain. The curves in Fig. 27 have two peaks for each sample: the first peak is related to the energy absorbed by the SMA wires located in the front facesheet and the second peak is related to the energy absorbed by the SMA wires located in the back facesheet.

In the first stage, the projectile impacts the front facesheet; by increasing the SMA wires pre-strain, the energy absorbed by the wires increases 139%, 219%, and 249.2% in the SGE-3W3, the SGE-3W6, and the SGE-3W8 samples, respectively, compared to the SGE-3W0 sample. In the second step, after the projectile impacts the back facesheet, the energy absorbed by the SMA wires located in the back facesheets increases by 17.21%, 61.8%, and 79.75%
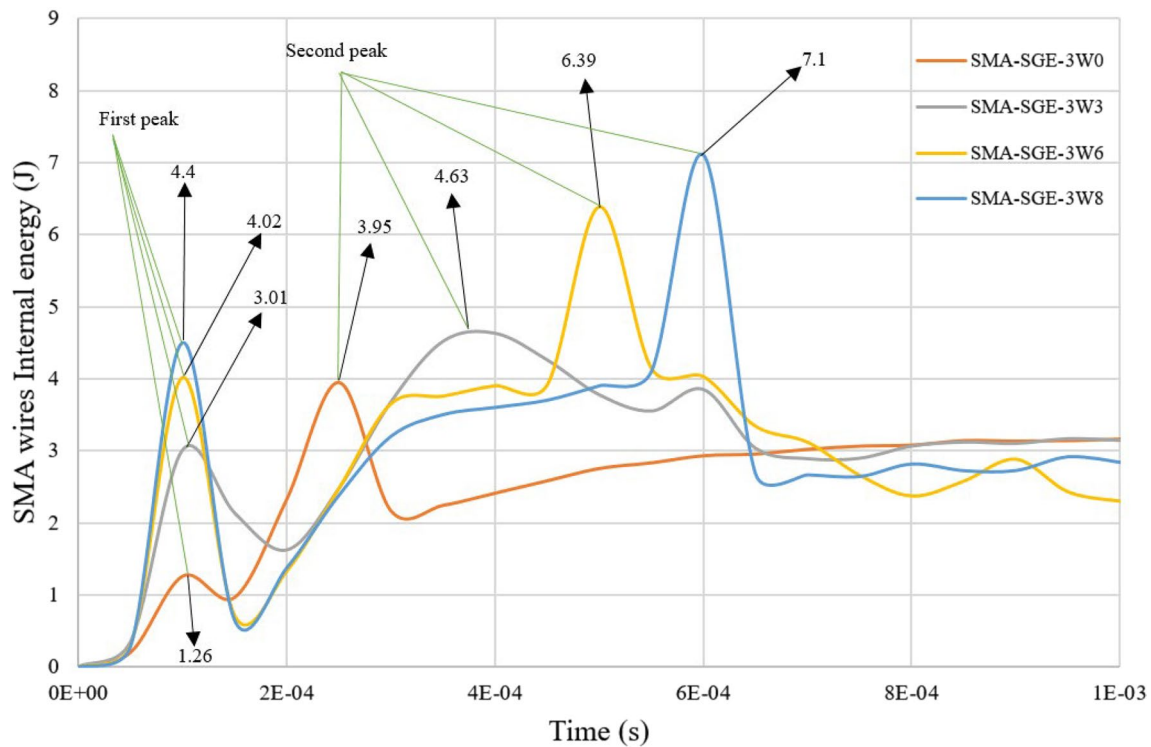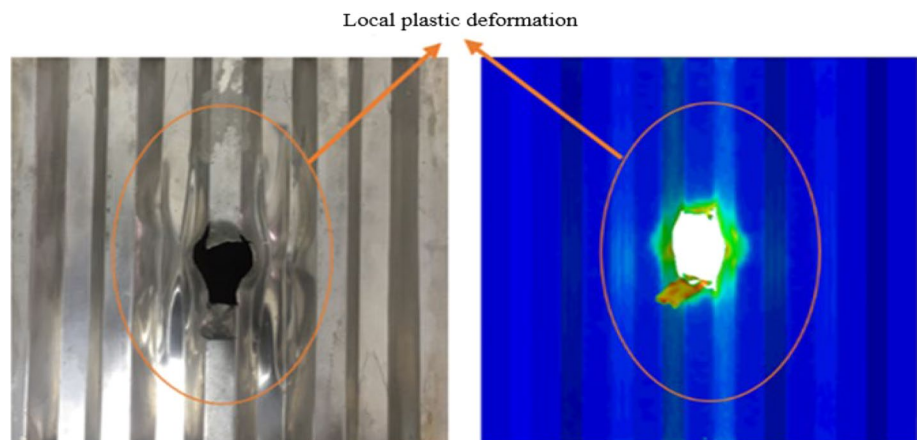
Fig. 27 Internal energy for shape memory wires in SGE-3W0, SGE-3W3, SGE-3W6, and SGE-3W8 samples

Fig. 28 Plastic deformation in SGE-3W3 core

in the SGE-3W3, the SGE-3W6, and the SGE-3W8 samples, respectively, compared to the SGE-3W0 sample.

Due to an increase in the wire's pre-strain, the SMA wires become softer and the impact resistance of the wires increases and the impact shock decreases. Thus, the second peaks move to the right in Fig. 27, and the projectile's impact duration with the wire's pre-strains increases. Then the shocking effect is reduced in the back facesheets. The results showed that the energy absorption by the SMA wires located in the back facesheets is greater than the energy absorbed by the SMA wires located in the front facesheets.

The reason is that the initial speed of the projectile reduces due to the impact of the front facesheet.

4.9 Impact on aluminum corrugated core

For a more in-depth study on the failure mode of aluminum corrugated core, the facesheets of SGE-3W3 samples were carefully debonded from the core. By comparing the experimental and numerical results obtained from the SGE-3W3 sample and ensuring the validity of the numerical results, a parametric study of other samples was done numerically.

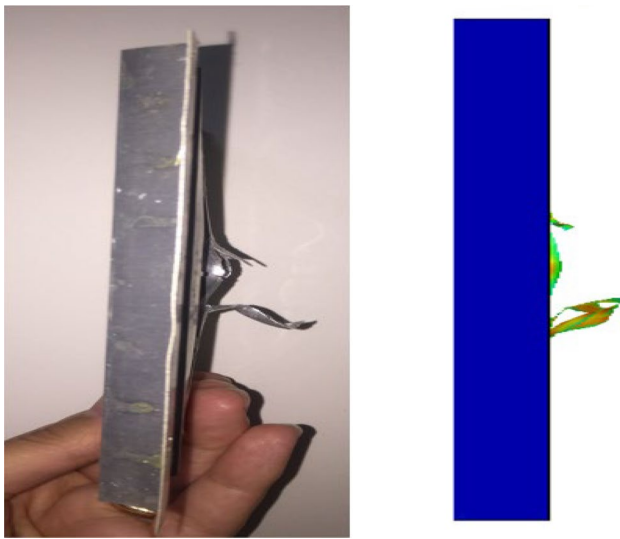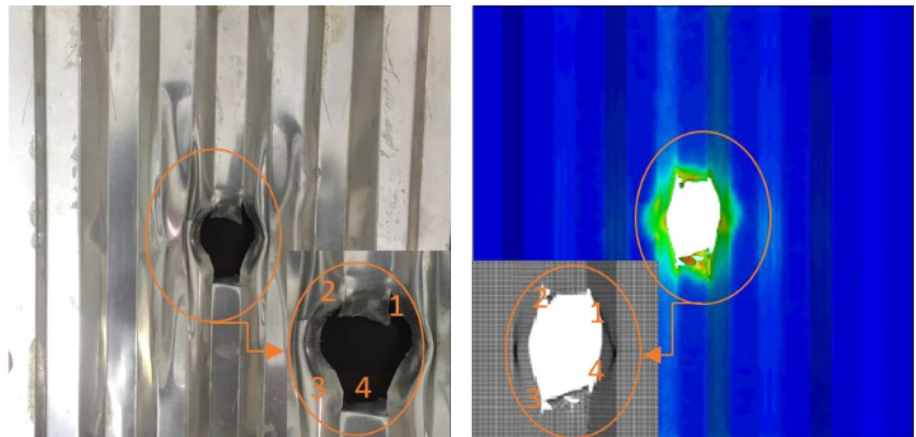**Fig. 29** Crack growth in SGE-3W3 core

Fig. 30 Core fracture in SGE-3W3 sample

Figures 28, 29, 30 show numerically and experimentally the plastic deformation of the core in the SGE-3W3 sample after impact. Initially, the energy is stored by the elastic deformation. After plastic deformation and exceeding the ultimate stress in the aluminum core, failure occurs in the core. As the projectile passes through the core, some energy is lost due to the friction between the core and the projectile. Additionally, some of the kinetic energy of the projectile is spent to overcome the bond between the core and the facesheets, which was locally visible around the impact point.

As demonstrated in Fig. 28, after the projectile hits and passes through the corrugated core, local plastic deformations formed around the impact point. This plastic deformation often leads to the separation of the core from the back facesheet at the plastic deformation zone. Figure 29 shows four cracks exactly developed at the bending point of the core. As a result of stress concentration in the bent places,
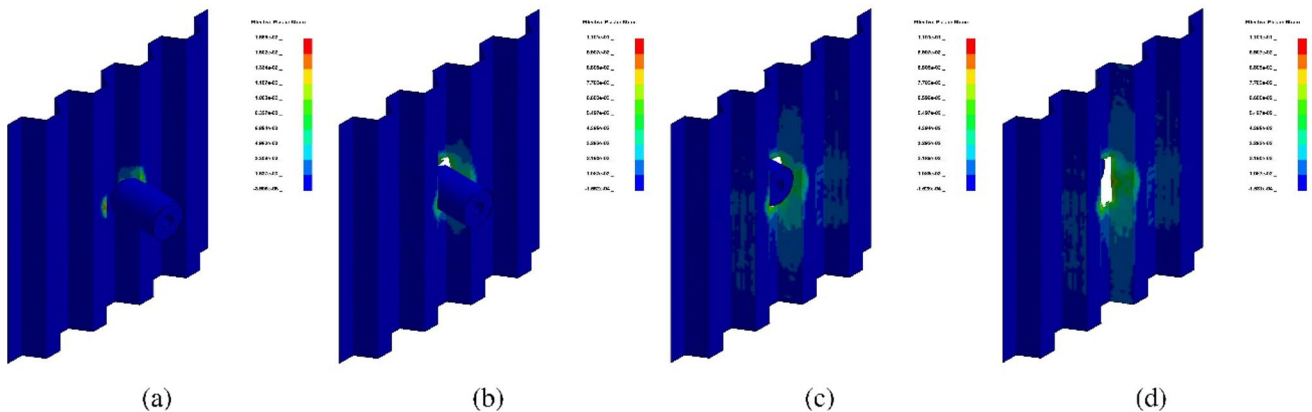

Fig. 31 Penetration of the impactor with an initial speed of 119 m/s in the GE-0W0 core at moments (**a**) 0.05 µs (**b**) 0.2 µs (**c**) 0.5 µs and (**d**) 0.7 µs
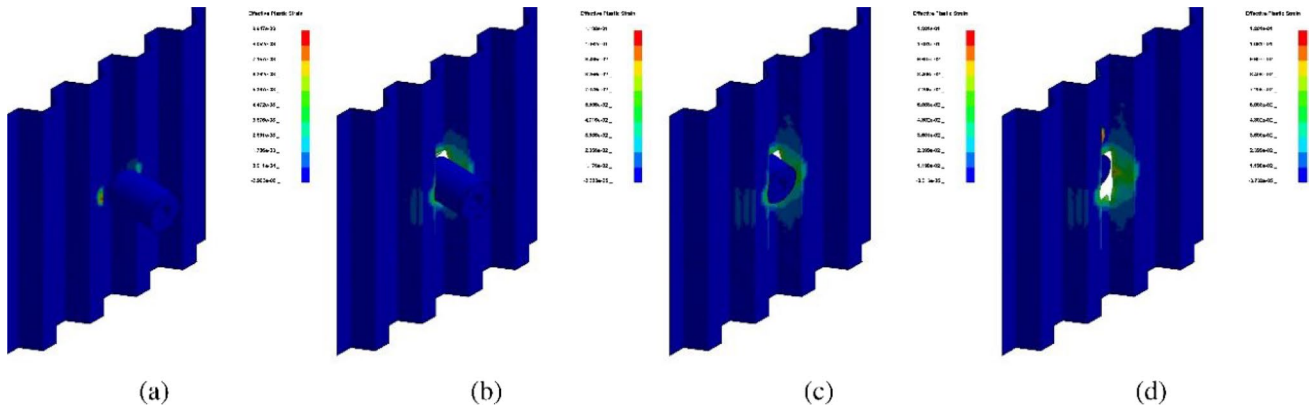
Fig. 32 Penetration of the impactor with an initial speed of 119 m/s in the SGE-3W0 core at moments (**a**) 0.05 μs (**b**) 0.2 μs (**c**) 0.5 μs and (**d**) 0.7 μs
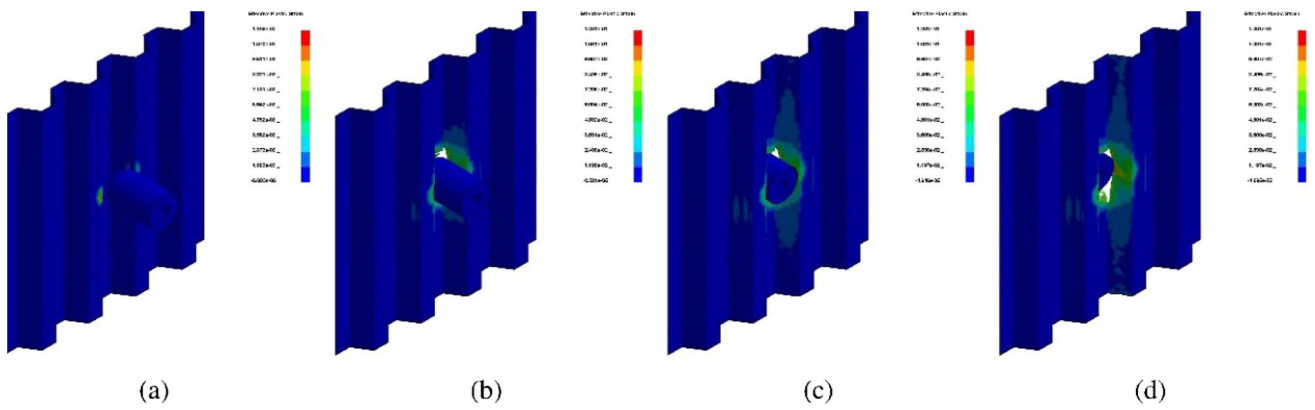

Fig. 33 Penetration of the impactor with an initial speed of 119 m/s in the SGE-3W3 core at moments (**a**) 0.05 μs (**b**) 0.2 μs (**c**) 0.5 μs and (**d**) 0.7 μs
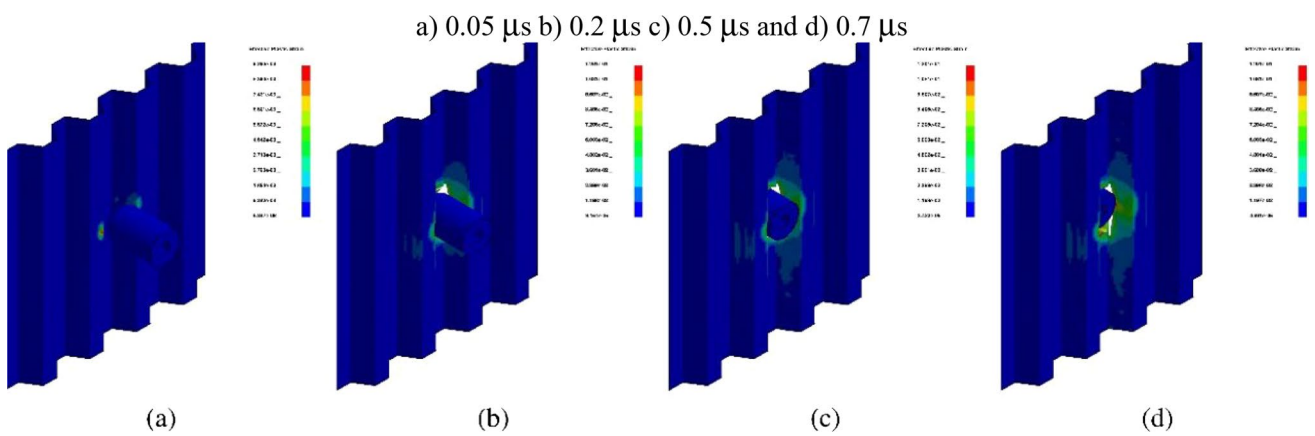
a) 0.05 μs b) 0.2 μs c) 0.5 μs and d) 0.7 μs

Fig. 34 Penetration of the impactor with an initial speed of 119 m/s in the SGE-3W6 core at moments (**a**) 0.05 μs (**b**) 0.2 μs (c) 0.5 μs and (d) 0.7 μs
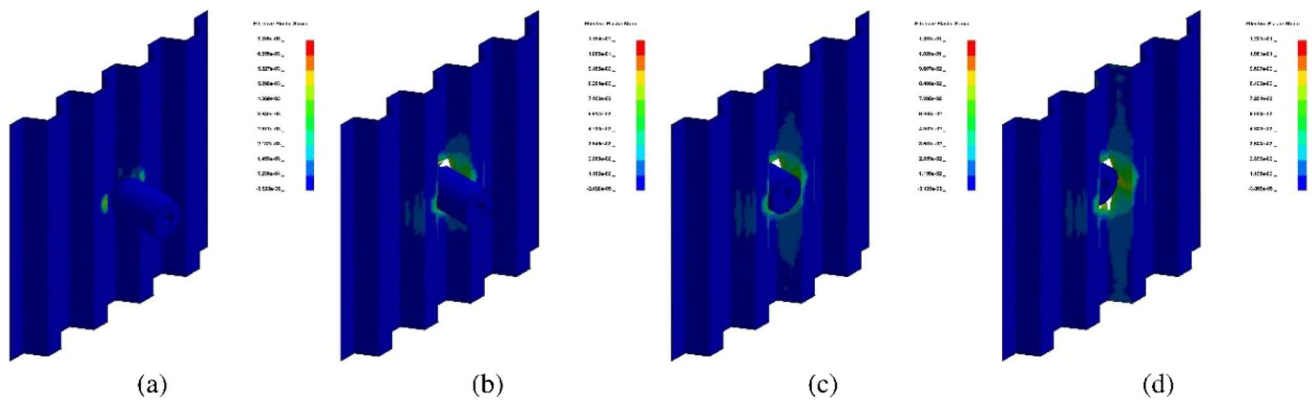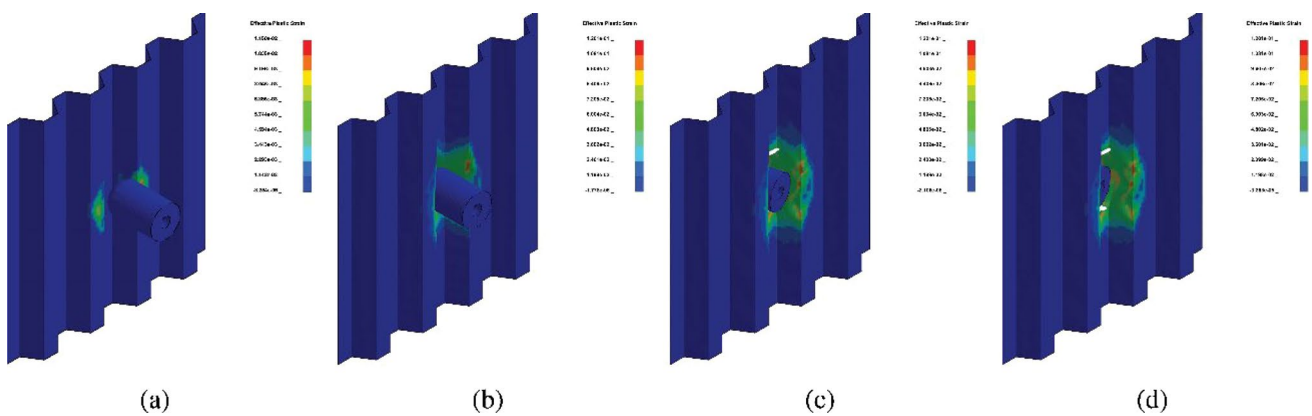
Fig. 35 Penetration of the impactor with an initial speed of 119 m/s in the SGE-3W8 core at moments (**a**) 0.05 µs (**b**) 0.2 µs (**c**) 0.5 µs and (**d**) 0.7 µs

Fig. 36 Penetration of the impactor with an initial speed of 119 m/s in the SGE-6W0 core at moments (**a**) 0.05 µs (**b**) 0.2µs (**c**) 0.5 µs and (**d**) 0.7 µs

cracks appeared and spread along the bend line after the projectile hit the aluminum corrugated core.

As shown in Fig. 30, when the projectile penetrates through the structure, the core began to rupture, and then petals are formed in the direction of the corrugated wave leading to form breaks and ruptures of composites in the back facesheet. The failure mechanism for the cores of all samples is almost similar. Figures 31, 32, 33, 34, 35, 36 show the plastic deformation of the cores at different intervals for various samples.

The results presented in Figs. 31, 32, 33, 34, 35, 36 show that the projectile first strikes the waves of the corrugated cores and causes deformation in the waves. At this stage, the deformation of the core and the friction created between the core and the projectile result in energy absorption. Then, the projectile hits the lower surface of the core; it ruptures and penetrates through the core. During this stage, the plastic deformation and, eventually, rupture of the core culminates with energy absorption. In corrugated cores, more energy is absorbed into the structure during these steps.

4.9.1 Ballistic limit speed

As mentioned in the previous section, in order to study the effect of applying pre-strain to the SMA wires located in the facesheets of sandwich panels, two configurations of smart sandwich panels with embedded SMA wires in the facesheets were considered (the samples with 3 and 6 SMA wires in each facesheet) and compared with samples without the SMA wire. This section presents a numerical simulation performed at different impact velocities to predict the ballistic limit speed for each sample. The ballistic limits which were obtained with different initial velocities are found to be about 82, 87.5, 97, and 85 m/s for GE-0W0, SGE-3W0, SGE-3W3, and SGE-6W0 samples by the polynomial trendline, respectively. The Vr verses Vi diagrams for different initial velocities are shown in Fig. 37.

As shown in Fig. 37, the SGE-3W3 sample, whose SMA wires have a pre-strain by 3%, has the best ballistic performance in comparison with the GE-0W0 and the SGE-3W0 samples. It was found that embedding the SMA wires in the
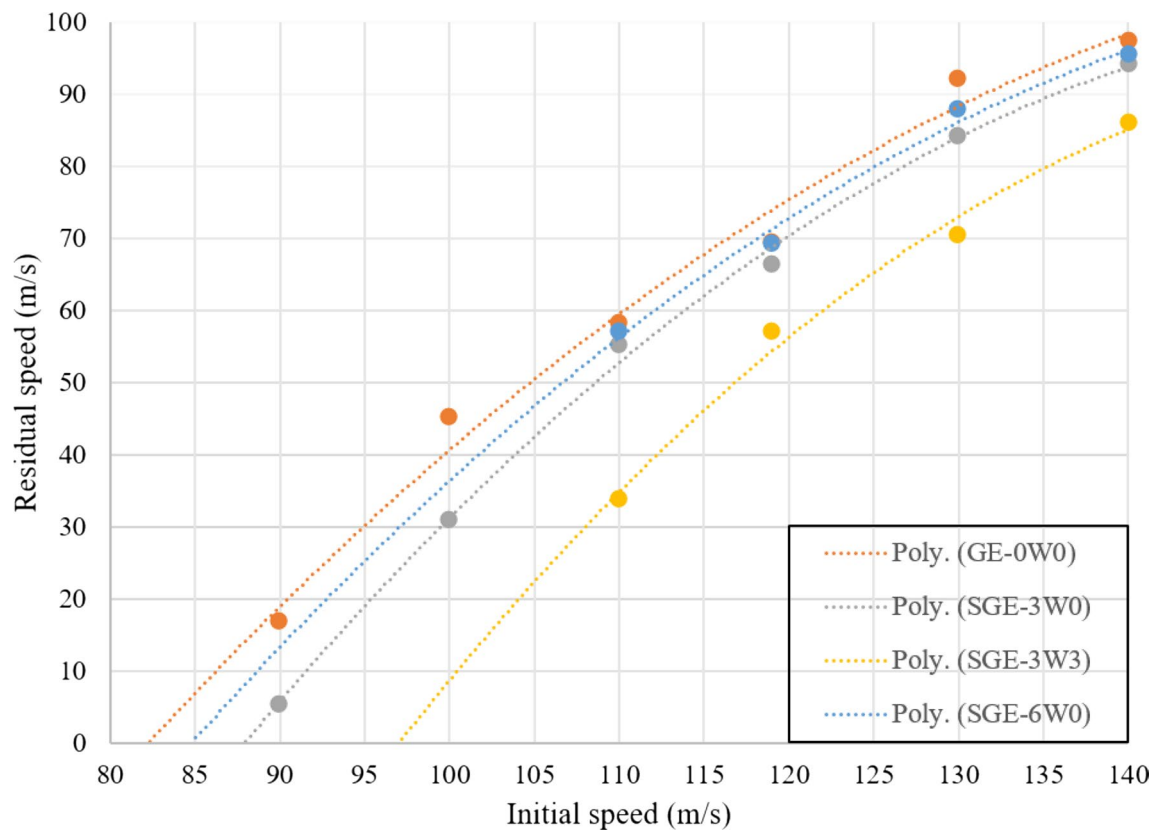
Fig. 37 Numerical comparison of residual speed versus impact speed

composite facesheets improves the ballistic performance. Moreover, applying the pre-strain to the SMA wires leads to a decrease in the residual speed in the same projectile's initial speed, and hence better high strain rate behavior.

5 Conclusion

The effect of high-speed impact on sandwich panels with the aluminum corrugated core and composite facesheets reinforced with superelastic SMA has been investigated numerically and experimentally in the present research. The study measures the effect of the quantity of shape memory alloy wires, the position of wires, and the percentage of wire pre-strain on impact phenomena such as limited speed, residual speed, and energy absorption by the sandwich panel structures as the variables. To explore the influence of the quantity of SMA wires, the following samples were made and tested: samples without SMA wires, 3-SMA wires in each facesheet, and 6 SMA wires in each facesheet. For the purpose of examining the effect of the SMA wire position, the wire is placed precisely at the point of impact in the 3 SMA wires sample; additionally, the impact occurred at the point where the middle wires are embedded. The effect of SMA

wire pre-strain on impact behaviors was studied by testing 3 SMA wires samples with 0% and 3% pre-strain. To validate the results, the finite element model was tested for all samples, and data were fed into LS-DYNA for simulation and validation. By validating the numerical analyses with experimental results, the contact force which exists between the projectile and the sandwich panels, the effect of pre-strain on SMA wires energy absorption, the aluminum corrugated core failure mechanism, and ballistic limit speed for various samples are investigated numerically. Furthermore, the failure mechanism is described in three stages for each of the sandwich panel components. It was found that when the SMA wires are located in the facesheets, the sandwich panel absorbs more energy compared with the sample without the SMA wires. Furthermore, adding pre-strain to the wires leads to increasing the absorption of energy in the sandwich panel. On the other hand, locating the SMA wire at the hitting point has more efficiency in increasing the absorbed energy.

The summary of conclusions is as follows:

1. The absorbed energy by composite facesheets increases by adding the SMA wires without pre-strain. The energy absorbed increases from 117.247J in GE-0W0 to 128.75J

and 142.5J for SGE-3W0, and SGE-3W3 samples, respectively.

2. Adding pre-strain decreases the projectile's residual speed. The projectile's residual speed of SGE-3W3 sample is 13.3% less than that of the SGE-3W0 sample.

3. Placing the SMA wires at the exact point of the projectile impact, would result in a greater effect on reducing the projectile's output speed. Absorbed energy by the SGE-3W0 sample is 4.6% greater than that for the SGE-6W0 sample.

4. Adding pre-strain to the wires, the contact time between the projectile and the SMA wires increases, and the impact shock effect decreases.

5. The energy absorbed by the composite facesheets increases by embedding the SMA wires in the composite facesheets.

6. SMA wires with pre-strain absorb more energy compared to SMA wires without pre-strain. By applying pre-strain, the maximum contact force occurred later and the total contact time increases, which results in minimizing the impact shocking effect in the sandwich structures and better behavior to high strain rate loadings.

Declarations

Conflict of interest The authors have no competing interests to declare that are relevant to the content of this article.

References

1. Luchinsky DG, Hafiychuk V, Smelyanskiy V, Tyson R, Walker JL, Miller JL (2011) "High-fidelity modeling for health monitoring in honeycomb sandwich structures" in Aerospace Conference. IEEE 2011:1–7

2. Shahbazi A, Zeinedini A (2021) Impact response of E-glass/epoxy composite Bi-directional corrugated core sandwich panels. Polym Polym Compos 29(9):1563–1574

3. Zhao H, Elnasri I, Girard Y (2007) Perforation of aluminium foam core sandwich panels under impact loading—An experimental study. Int J Impact Eng 34:1246–1257

4. Wang Z (2019) Recent advances in a novel metallic honeycomb structure. Compos Part B: Eng 166:731–741

5. Ivañez I, Santiuste C, Barbero E, Sanchez-Saez S (2011) Numerical modeling of foam-cored sandwich plates under high velocity impact. Compos Struct 93(9):2392–2399

6. Nettles AT, Lance DG (1993) On the enhancement of impact damage tolerance of composite laminates. Compos Eng 3(5):383–394

7. Wang D (2009) Impact behavior and energy absorption of paper honeycomb sandwich panels. Int J Impact Eng 36(1):110–114

8. Tipping S, Stojadinovic B (2008) Innovative corrugated steel shear walls for multi-story residential buildings. In: The 14th World Conference on Earthquake Engineering, pp 12–17

9. Ning H, Janowski GM, Vaidya UK, Husman G (2007) Thermoplastic sandwich structure design and manufacturing for the body panel of mass transit vehicle. Compos Struct 80(1):82–91

10. McGowan D, Ambur DR (1997) Damage-tolerance characteristics of composite fuselage sandwich structures with thick face sheets. In: NASA Technical Memorandum 110303

11. Heimbs S, Middendorf P, Hampf C, Hähnel F, Wolf K (2008) Aircraft sandwich structures with folded core under impact load. In: Proc. of the 8th International Conference on Sandwich Structures, ICSS8, Porto, Portugal

12. Alkhatib SE, Matar MS, Tarlochan F, Laban O, Mohamed AS, Alqwasmi N (2019) Deformation modes and crashworthiness energy absorption of sinusoidally corrugated tubes manufactured by direct metal laser sintering. Eng Struct 15(201):109838

13. Buehler WJ, Wiley RC, Wang FE (1965) Nickel-base alloys. US patent 3(174):851

14. Song G, Ma N, Li HN (2006) Applications of shape memory alloys in civil structures. Eng Struct 28(9):1266–1274

15. Rogers CA, Robertshaw HH (1988) Shape memory alloy reinforced composites. Eng Sci Preprints (Soc Eng Sci) 25:20–22

16. Abrate S (1994) Impact on laminated composites: recent advances. Appl Mech Rev 47:517–544

17. Olsson R (2003) Closed form prediction of peak load and delamination onset under small mass impact. Compos Struct 59(3):341–349

18. Karthikeyan K, Russell BP, Fleck NA, Wadley HN, Deshpande VS (2013) The effect of shear strength on the ballistic response of laminated composite plates. Eur J Mech-A/Solids 42:35–53

19. Khalili SMR, Hosseini M, Fard KM, Forooghy SH (2013) Static indentation response of an in-plane prestressed composite sandwich plate subjected to a rigid blunted indenter. Eur J Mech-A/Solids 38:59–69

20. Sahoo SS, Panda SK, Mahapatra TR (2016) Static, free vibration and transient response of laminated composite curved shallow panel–an experimental approach. Eur J Mech-A/Solids 59:95–113

21. Katariya PV, Mehar K, Panda SK (2020) Nonlinear dynamic responses of layered skew sandwich composite structure and experimental validation. Int J Non-Linear Mech 1(125):103527

22. Cantwell WJ, Morton J (1989) Comparison of the low and high velocity impact response of CFRP. Composites 20:545–551

23. Cantwell WJ, Morton J (1990) Impact perforation of carbon fibre reinforced plastic. Compos Sci Technol 38:119–141

24. Cantwell WJ, Morton J (1989) The influence of varying projectile mass on the impact response of CFRP. Compos Struct 13:101–114

25. Tanabe Y, Aoki M, Fujii K, Kasano H, Yasuda E (2003) Fracture behavior of CFRPs impacted by relatively high-velocity steel sphere. Int J Impact Eng 28:627–642

26. Hazell PJ, Kister G, Stennett C, Bourque P, Cooper G (2008) Normal and oblique penetration of woven CFRP laminates by a high velocity steel sphere. Compos A 39:866–874

27. Hazell PJ, Cowie A, Kister G, Stennett C, Cooper GA (2009) "Penetration of a woven CFRP laminate by a high velocity steel sphere impacting at velocities up to 1875 m/s. Int J Impact Eng 36:1136–1142

28. Hazell PJ, Appleby-Thomas GJ (2012) The impact of structural composite materials. Part 1: ballistic impact. Strain Anal 47:396–405

29. Appleby-Thomas GJ, Hazell PJ (2012) The impact of structural composite materials. Part 2: hypervelocity impact and shock. Strain Analy 47:406–418

30. Gower HL, Cronin DS, Plumtree A (2008) Ballistic impact response of laminated composite panels. Int J Impact Eng 35:1000–1008

31. He HM, Wen Y (2008) QIN, "Finite element analysis to predict penetration and perforation of thick FRP laminates struck by projectile." Int J Impact Eng 35:27–36

32. López-Puente J, Zaera R, Navarro C (2008) Experimental and numerical analysis of normal and oblique ballistic impacts on thin carbon/epoxy woven laminates. Compos A 39:374–387

33. Wadley HN, Børvik T, Olovsson L, Wetzel JJ, Dharmasena KP, Hopperstad OS, Deshpande VS, Hutchinson JW (2013) Deformation and fracture of impulsively loaded sandwich panels. J Mech Phys Solids 61(2):674–699

34. Kılıçaslan C, Güden M, Odacı IK, Taşdemirci A (2013) The impact responses and the finite element modeling of layered trapezoidal corrugated aluminum core and aluminum sheet interlayer sandwich structures. Mater Design 46:121–133

35. Ma Q, Rejab MR, Siregar JP, Guan Z (2021) A review of the recent trends on core structures and impact response of sandwich panels. J Compos Mater 55(18):2513–2555

36. Khalili SMR, Shokuhfar A, Malekzadeh K, Ghasemi FA (2007) Low-velocity impact response of active thin-walled hybrid composite structures embedded with SMA wires. Thin-Walled Struct 45(9):799–808

37. Shokuhfar A, Khalili SMR, Ghasemi FA, Malekzadeh K, Raissi S (2008) Analysis and optimization of smart hybrid composite plates subjected to low-velocity impact using the response surface methodology (RSM). Thin-Walled Struct 46(11):1204–1212

38. Eslami-Farsani R, Khazaie M (2018) Effect of shape memory alloy wires on high-velocity impact response of basalt fiber metal laminates. J Reinf Plast Compos 37:300–309

39. Verma L, Sivakumar SM, Andrew JJ, Balaganesan G, Arockirajan A, Vedantam S (2019) Compression after ballistic impact response of pseudoelastic shape memory alloy embedded hybrid unsymmetrical patch repaired glass-fiber reinforced polymer composites. J Compos Mater 53(28–30):4225–4247

40. Paine J, Rogers C (1995) High velocity impact response of composites with surface bonded nitinol-SMA hybrid layers. In: Proceeding of 36th Structures, Structural Dynamics and Materials Conference, pp 2084–2094

41. ASTM International. Committee B07 on Light Metals and Alloys. Standard test methods for tension testing wrought and cast aluminum-and magnesium-alloy products (Metric). ASTM International; 2015.

42. ASTM D. 3039. Standard test method for tensile properties of polymer matrix composite materials. 2014.

43. Standard AS. D5379–05, 2005. "Standard Test Method for Shear Properties of Composite Materials by the V-Notched Beam Method", West Conshohocken, PA, 2005, DOI: https://doi.org/10.1520/D5379-05.

44. Standard AS. D6641–09, 2009. "Standard Test Method for Compressive Properties of Polymer Matrix Composite Materials Using a Combined Loading Compression (CLC) Test Fixture", West Conshohocken, PA, 2008, DOI: https://doi.org/10.1520/D6641-09.

45. Lagoudas DC (2008) Shape memory alloys: modeling and engineering applications. Springer Science & Business Media, Berlin

46. Hallquist JQ (2007) LS-DYNA user manual version 971", Livermore Software Technology Corp, Livermore

47. Wade B, Feraboli P, Osborne M (2012) Simulating laminated composites using LS-DYNA material model MAT54 part I: [0] and [90] ply single-element investigation", In: FAA Joint Advanced Materials and Structures (JAMS) Centre of Excellence, Technical Review Meeting, MD

48. L.-D.K.U.s. Manual, II. Volume, Livermore Software Technology Corporation, 2018, p. 398. Version 11.

49. Spranghers K, Kakogiannis D, Ndambi JM, Lecompte D, Sol H (2010) Deformation measurements of blast loaded plates using digital image correlation and high-speed photography. EPJ Web Conf 6:12006. https://doi.org/10.1051/epjconf/20100612006

50. Gur S, Mishra SK, Frantziskonis GN (2016) Thermo-mechanical strain rate-dependent behavior of shape memory alloys as vibration dampers and comparison to conventional dampers. J Intell Mater Syst Struct 27(9):1250–1264

51. Adharapurapu RR, Jiang F, Vecchio KS, Gray GT (2006) Response of niti shape memory alloy at high strain rate: a systematic investigation of temperature effects on tension-compression asymmetry. Acta Mater 54(17):4609–4620

52. Wentao H, Jingxi L, Bo T, De X, Jiayi L, Zhang M (2016) Experimental and numerical research on the low velocity impact behavior of hybrid corrugated core sandwich structures. Compos Struct 158:30–43

53. Maher R, Khalili SM, Eslami-Farsani R (2022) Experimental analysis of corrugated core sandwich panel with smart composite face-sheets under high-velocity impact. J Compos Mater 56(10):1495–1511

54. Jiga G, Stamin S, Dinu G (2018) Behavior of composite sandwich panels with several core designs at different impact velocities. In: AIP Conference Proceedings, (Vol. 1932, No. 1, p. 030040). AIP Publishing LLC.